



POLITECNICO DI TORINO

In fulfilment of the requirements for the master's degree
in Nanotechnology Engineering

Tesi di Laurea Magistrale

Simulation of GaN-based LEDs and solar cells

Correlating quantum-corrected models and experimental characterizations

Supervisor:

Prof. Michele GOANO

Candidate:

Lorenzo AVATANEO

Co-supervisors:

Dr. Alberto TIBALDI

Prof. Francesco BERTAZZI

Dr. Pierluigi DEBERNARDI

In Collaboration with the Department of Information Engineering
of the University of Padova

December 2019

Introduction

Nitride alloys have emerged as the most promising semiconductor compounds for ultraviolet (UV) applications. GaN-based LEDs are of particular interest in the medical environment, as the use of UV light for disinfection in clinical settings and for catalyzing chemical reactions. Color-coded LED microscopy (cLEDscope) is a novel computational microscopy technique capable of multi-contrast and quantitative phase imaging of biological specimens using color-multiplexed illumination [1]. GaN-based solar cells find their main application when incorporated in multi-junction photovoltaic structures which can provide high theoretical conversion efficiencies. The InGaN band gap engineering, performed by varying the In molar fraction, permits the light emission and absorption in the near UV range. In addition, it has been demonstrated that these solar cells exhibit excellent thermal stability and high-energy-proton radiation resistance, which makes them suitable to be used in harsh environments such as concentrated sunlight and space applications. However, most of the reported InGaN-based solar cells are not as efficient as expected, mostly due to the difficulty of growing high crystalline quality InGaN alloys [2]. It has been observed that multi-quantum-well (MQW) active regions show an obvious advantage in terms of structural quality [3].

This thesis investigates the performances of state-of-the-art GaN-based light emitting diodes (LEDs) and solar cells through experimental characterizations and simulations. The measurements performed on the LED samples and solar cells have been provided by the Department of Information Engineering (DIE) of the University of Padova, courtesy of *Nicola Renso, Alessandro Caria, Matteo*

Meneghini, Carlo De Santi et al.. The experimental results reported in the thesis include current-voltage (IV) characteristics, electroluminescence (EL) spectra and light-current (LI) measurements. Moreover, the thermal behaviour of the LED samples is analyzed through thermally-controlled measurements from cryogenic temperatures to 350K. The experimental results are interpreted through the comparison with the results of a campaign of parametric simulations based on a quantum-corrected drift-diffusion electro-optical model.

The investigated opto-electronic devices are based on InGaN/GaN MQW active regions and AlGaN electron blocking layers (EBLs). The role of the EBL is investigated in detail, demonstrating how it can enhance the spontaneous emission in the active region of a GaN-based LED or improve the extraction of the photogenerated carriers in a GaN-based solar cell.

The main purpose of this thesis is to achieve a better understanding of the physical behaviour of GaN-based devices. In addition to effects appearing in typical III-V optoelectronic devices such as band gap renormalization due to coulombian interactions in the QWs, current crowding, or the uncertainty given by the composition fluctuations inside the wells, a proper description of nitride-based devices requires to account for physical effects peculiar of these material systems. Among these, the most noticeable is the presence of polarization fields at the GaN/InGaN heterointerfaces, related to the spontaneous polarization of III-N wurzite materials and induced by the lattice mismatch at the interfaces.

This thesis consists of three chapters. The first is completely dedicated to the analysis of the GaN-based LEDs at room temperature and the relative simulations. In order to fit the experimental IV characteristics, the first step is to assess the impact of the polarization fields. This is achieved by determining the polarization screening factor with respect to the Bernardini-Fiorentini model [4]. The simulations performed in this thesis are based on 1D models, so that current crowding effects are taken into account by introducing series resistances. For what concerns the EL spectra, achieving a good match between experiments and simulations is more complex because of the number of possible dependences: the In molar fraction in the wells, the thicknesses of the QWs, the interface charges and the band gap renormalization. Moreover, the efficiency droop is verified both experimentally and theoretically.

In the second chapter the temperature behaviour of the LEDs is reported. A collection of temperature dependences of the main parameters of the simulations is introduced in order to pursue a complete modelization in temperature. The matching of the IV characteristics in a wide range of temperature is obtained by extrapolating the thermal dependence of the interface charges and the series resistance. The experimental EL spectra show an unconventional thermal behaviour not predicted by the simulations that is partially in accord with the literature. In fact, a debate on the efficiency droop (efficiency decreasing with the current injection) and the thermal droop (efficiency decreasing with the temperature) in GaN-based LEDs has characterized the last decade. For this reason, a deeper study is carried out on the different phenomena that could justify the experimental evidences.

In the third and last chapter the attention is focused on the GaN-based MQW solar cells. After a preliminary introduction on the characterization of the performances, the complex geometries of the photovoltaic structures are presented. A comparison between the EL spectra is performed in order to check the degree of quality of the active regions. Then the performances under AM1.5g illumination are commented. The effect of the EBL is questioned by the decrease in terms of simulated performances. Moreover, a decrease in absorption in the active regions is verified by the models with thicker p-GaN cladding layers or smaller number of QWs.

Besides the three main chapters it seemed necessary the addition of two extra appendices to give a close view to the material properties of the nitride alloys and the simulative process. The first appendix contains all the relevant properties of the nitride alloys. The wurtzite lattice structure is investigated and connected to the spontaneous polarization, while the presence of the piezoelectric polarization is correlated to the lattice mismatch between the interfaces. Then the model of the interface charges defined by *Fiorentini et al.* is depicted, since it is the one used by the commercial simulator. Additional information are given about the InGaN band gap engineering through the variation of the In molar fraction. Then the final sections are related to the technological processes of GaN crystal growth, doping and contact development.

The second and last appendix describes the core of the simulations, starting

from the drift-diffusion model and connecting the quantum corrections to the iterative procedure through the Schrödinger equation. The recombination processes are then listed following the ABC model, being the key for a coherent simulation of this kind of devices. Finally, the material parameters used to modelize the nitride alloys are listed in order to permit a straightforward reproduction of the simulated results.

Hoping that this thesis will not only be of interest for the experts of the field, in the appendices can be found all the information needed to understand the mechanics of this work. The intent, based on the previous knowledge of the reader, is to provide two possible ways of looking through the chapters. By following the given order of sections, the reader can be immediately catapulted in the core of the work and his reading can be supported by the several references present in the text. Otherwise, if necessary, the reader can firstly dedicate some time to the information given in the appendices so to acquire the tools that will allow him to fully understand the research. Hopefully, either way, the reader will be able to understand the results obtained and to appreciate the possible applications this work can lead to.

List of Figures

1.1	Cross section of each LED structure under study. Only one half of the structure is reported, thanks to the symmetry along the lateral direction \vec{x} . The symmetry axis at the center of each mesa is represented as a dotted line. The figure is not drawn to scale.	2
1.2	[T=298 K] Experimental IV characteristics (logarithmic scale) of the LEDs and differential resistances. The ideality factor is reported in the side plot (current in logarithmic scale).	4
1.3	[T=298 K] Experimental IV characteristics (logarithmic scale) of the LEDs and total optical power in arbitrary unit.	6
1.4	[T=298 K] Experimental EL spectra given for a discreet set of current values: $20 \mu\text{A}$, $50 \mu\text{A}$, $100 \mu\text{A}$, $200 \mu\text{A}$, $500 \mu\text{A}$, 1 mA , 2 mA , 5 mA , 10 mA , 20 mA , 50 mA . The intensities are in arbitrary units.	8
1.5	[T=298 K] (a) Total optical power in arbitrary unit (logarithmic scale). (b) EQE in arbitrary unit.	10
1.6	Simulated 1D geometry of structure A. The apparent width of the column-shaped device along the \vec{x} direction is fixed to $500 \mu\text{m}$. The figure is not drawn to scale.	11
1.7	(a) Band diagram of structure A at equilibrium with confined states of the QWs and carrier concentrations. The QWs and the EBL are highlighted with light colors, the colors of the QWs are related to their optical emission. (b) Band diagram of structure A at 4 V, figure depicted as the one at equilibrium.	15

1.8	(a) Comparison of the electron concentrations at 4 V in the three LED structures. The two QWs are highlighted in light gray and the EBL in light blue. (b) Comparison of the hole concentrations; figure depicted as (a).	16
1.9	IV characteristic curve and differential resistance of structure A (logarithmic scale). Comparison with the experimental results and the dependence of the fraction of polarization charges are presented. The simulator reports the IV characteristic in Am^{-1} , multiplying by W we obtain the curve in figure.	17
1.10	(a) Comparison of the EL intensities: experimental at 50 mA, simulated at 4 V. The vertical lines select the wavelengths related to the nominal and effective energy gaps. (b) Radiative recombination spatially resolved.	19
1.11	(a) Normalized EL intensity, dependence on the In molar fraction inside the QWs. Overlap with 0.11 for the blue QW and 0.25 for the green QW. (b) Normalized EL intensity, dependence on the thickness of the QWs. (c) Normalized EL intensity, dependence on the fraction of polarization charges. (d) Not normalized EL intensity, dependence on the fraction of polarization charges.	20
1.12	Effect of the coulombian interactions on the EL spectrum of structure A, B and C. The exchange coefficient has been applied with a value of 8×10^{-8} eVcm for all the three structures.	21
1.13	Experimental total optical power and EQE of structure C as a function of the current injection. Simulated internal optical power of structure C and simulated IQEs of the three structures with $x_{pol} = 0.6$. 23	
2.1	Temperature dependent IV characteristics, experimental measurements in solid lines, simulated results as scattered plot (logarithmic scale). Experimental temperature dependent ideality factor in the side plot (current axis in logarithmic scale).	29
2.2	(a) Extrapolated temperature trend of the contact resistance $R_c(T)$ with fitting curve. (a) Extrapolated temperature trend of the fraction of polarization charges $x_{pol}(T)$ with fitting curve.	30

2.3	(a) Experimental (dotted lines) and simulated (dashed lines) EL intensities as a function of the temperature at 100 mA, both reported in arbitrary unit and not comparable in terms of absolute value. (b) EL intensities at 5 mA. Fig. (a) and (b) are comparable. (c) Trend with respect to the temperature of the peaks at 100 mA. Simulated and experimental peaks are normalized to have agreement of the sum of the two peaks at 350 K. (d) Trend of the peaks at 5 mA. Fig. (c) and (d) are comparable, indeed the normalization used in (c) is kept.	33
2.4	(a) Evaluated experimental EQE with respect to the current flow for the range of temperature of the measured EL spectra. (b) Evaluated experimental EQE with respect to the temperature for the range of current values of the measured EL spectra.	34
2.5	(a) Fig. from <i>Wang et al.</i> [31]. (b) Fig. from <i>Shin et al.</i> [32]. (c) Fig. from <i>Shin et al.</i> [32]. (d) Fig. from <i>Han et al.</i> [44].	37
2.6	(a) Fig. from <i>Dalapati et al.</i> [45]. (b) Fig. from <i>Dalapati et al.</i> [45]. (c) Fig. from <i>Prudaev et al.</i> [46]. (d) Fig. from <i>Prudaev et al.</i> [47].	38
2.7	(a) Fig. from <i>Wang et al.</i> [48]. (b) Fig. from <i>Wang et al.</i> [49]. (c) Fig. from <i>Wang et al.</i> [49].	39
3.1	Simulated 1D geometry of structure 1C. The apparent width of the column-shaped device along the \vec{x} direction is fixed to $500\mu\text{m}$, however the results will be reported as quadratic densities. The figure is not drawn to scale.	44
3.2	[T=298 K] (a) Band diagram of structure C at 1.5 V with confined states of the QWs and carrier concentrations. (b) Band diagram of structure 2A at 1.5 V, figure depicted as the one at equilibrium. The QWs and the EBL are highlighted with light colors.	45
3.3	[T=298 K] Experimental and simulated EL intensities of the structures C and 2A. All data are normalized to the maximum peak. . .	46

3.4 [T=298 K] (a) JV characteristics under AM1.5g illumination. (b) AM1.5g solar spectrum; the two extremes of the yellow region are the wavelengths related to maximum peaks of EL intensity of structure C and 2A (zoom in the significant region in the side plot). 47

A.1 (a) Primitive cell of wurtzite GaN with nearest N atoms bounded. (b) Super-lattice in parallel projection with respect to *a* direction. Both crystal morphologies are produced using the 3D visualization program for structural models **VESTA** (Visualization of Electronic and SStructural Analysis). 54

A.2 Lattice constant vs energy gap of GaN, InN, AlN and the alloys. . . 55

A.3 GaN and InN energy gaps versus temperature. Dotted lines, energy gaps at the lower temperature achieved during reliability test. Dashed lines, energy gaps at room temperature. Dot-dashed lines, energy gaps at the highest experimental temperature. 56

A.4 InGaN nominal energy gap and related emission wavelength as a function of In concentration. Blue dashed line: $x_{\text{In}} = 0.10$, $E_g|_{\text{InGaN}} = 2.90 \text{ eV}$, $\lambda|_{\text{InGaN}} = 427.3 \text{ nm}$. Green dashed line: $x_{\text{In}} = 0.19$, $E_g|_{\text{InGaN}} = 2.46 \text{ eV}$, $\lambda|_{\text{InGaN}} = 503.5 \text{ nm}$ 57

List of Tables

1.1	Values of the polarization at the beginning of the photoluminescence, $20 \mu\text{A}$, and for the EL spectrum with highest current flow, 50 mA	6
1.2	Main parameters of the quantum corrected DD simulations.	12
1.3	Nominal energy gap and relative wavelength extracted from the dependence on the In molar fraction in Fig. A.4.	18
2.1	Modelization of thermal dependences of the main parameters used for the simulation at room temperature. It is recommended to read the section to understand the table.	26
3.1	Structure designs of the GaN-based solar cells.	43
3.2	Device performances of the InGaN/GaN MQW solar cells ([e/s] [QWs] [x_{pol}] = [experimental/simulated] [number of QWs] [fraction of polarization charges]). $x_{pol} = 0.4$ when not reported.	49
B.1	Parameters of the damped Newton method.	63
B.2	Material parameters of GaN, InN and AlN.	69

List of Acronyms

Si Silicon

In Indium

LH Light Hole

Ti Titanium

InN Indium Nitride

InGaN Indium Gallium Nitride

LED Light Emitting Diode

UV Ultra-Violet

O Oxygen

EL Electro-Luminescence

EBL Electron Blocking Layer

HBL Hole Blocking Layer

IQE Internal Quantum Efficiency

EQE External Quantum Efficiency

EXE Photon Extraction Efficiency

QW Quantum Well

MQW Multiple Quantum Well

Al Aluminium

AlGaN Aluminium Gallium Nitride

AlInN Aluminium Indium Nitride

Ga Gallium

Ge Germanium

N Nitrogen

H Hydrogen

Mg Magnesium

Au Gold

Ni Nickel

SiC Silicon Carbide

GaN Gallium Nitride

AlN Aluminium Nitride

NiO Nickel Oxide

DD Drift-Diffusion model

JV Current density versus Voltage characteristic

IV Current versus Voltage characteristic

FF Fill Factor

SRH Shockley-Read-Hall

TAT Trap-Assisted Tunneling

JDOS Joint Density Of States

QCSE Quantum Confined Stark Effect

HH Heavy Hole

HVPE Hydride Vapour Phase Epitaxy

MOCVD Metal Organic Chemical Vapour Deposition

MBE Molecular Beam Epitaxy

RHEED Reflection High-Energy Electron Diffraction

LEEBI Low Energy Electron Beam Irradiation

LI Light-Current

LIC Limiting Injection Current

Contents

1	InGaN/GaN Color-Coded LEDs	1
1.1	Experimental characterization	1
1.1.1	Mesa structures: QW position, $\text{Al}_x\text{Ga}_{1-x}\text{N}$ EBL	1
1.1.2	Experimental details	2
1.1.3	IV characteristics	3
1.1.4	Total optical power	5
1.1.5	Electro-luminescence spectrum	7
1.1.6	External quantum efficiency	7
1.2	Simulation analysis	11
1.2.1	1D modelization and simulation parameters library	11
1.2.2	Simulation results	14
2	InGaN/GaN LED temperature behaviour	25
2.1	Introduction	25
2.2	Selection of thermal dependences	25
2.3	IV characteristics	29
2.4	Investigation on the thermal droop	30
2.5	EL intensities	31
3	InGaN/GaN MQW solar cells	40
3.1	Introduction	40
3.2	Electrical characterization of a solar cell	40
3.3	Mesa structures: QW thickness, EBL and HBL	42
3.4	Analysis of the results	44

3.4.1	Performances under AM1.5g solar irradiance	47
4	Conclusions	50
A	InAlGaN material properties	53
A.1	Lattice structure	53
A.1.1	Polarization charges at the interfaces	53
A.2	Bandgap	56
A.3	GaN crystal growth techniques	58
A.4	GaN doping process	59
A.5	Contact development	60
B	Theory behind the simulations	61
B.1	Drift-diffusion model	61
B.1.1	Damped Newton method	62
B.2	Self-consistent carrier density model	63
B.3	ABC model	65
B.3.1	SRH recombination rate	65
B.3.2	Radiative recombination rate	66
B.3.3	Auger recombination rate	67
B.4	Generation rate	67
B.5	Incomplete ionization of impurities	68
B.6	GaN, InN, AlN parameter collection	68

InGaN/GaN Color-Coded LEDs

1.1 Experimental characterization

The first section of this chapter focuses on the description of the experimentally characterized GaN-based LEDs. Firstly, we will present the three different structures and we will then analyze the set of data received from the University of Padova.

1.1.1 Mesa structures: QW position, $\text{Al}_x\text{Ga}_{1-x}\text{N}$ EBL

As discussed in the introduction, the study in question focuses on a preliminary experimental analysis of the GaN-based LEDs and our study was carried out on three sets of nominally identical structures, the schematics of which are reported in Fig. 1.1. Here follows a description of the geometry of structure A and of the comparison to structure B and C.

Each wafer was fabricated pursuing a bottom to top technology process, then a selective etching was used to shape each electronic device in form of the so-called mesa structure. This name derives from the geomorphology area, where indicates an isolated flat-topped elevation with steep sides. The mesa structure was grown on top of a sapphire substrate, followed by a $3\ \mu\text{m}$ thick undoped GaN layer and a $1.5\ \mu\text{m}$ thick n-type GaN layer ($[\text{Si}] N_D = 5 \times 10^{18}\ \text{cm}^{-3}$). We then find the active region which consists of two InGaN QWs sandwiched by three GaN barrier layers. Starting from the bottom, the first barrier layer has a thickness of 20 nm while the other two of 10 nm. The first QW has a value of 0.19

In molar fraction whereas the second one 0.10, however only the former one is affected by an error of ± 0.01 as the manufacturing company has made known. A 20 nm thick AlGaN EBL ($N_A = 2 \times 10^{19} \text{ cm}^{-3}$) and a 200 nm thick p-type GaN layer ($[\text{Mg}] N_A = 2 \times 10^{19} \text{ cm}^{-3}$) were grown on top of the active region. The total width of the section standing up above the substrate is $500 \mu\text{m}$.

The structure B differs from A for the Al molar fraction in the EBL, which was decreased from 0.20 to 0.15. Instead, the structure C has the same EBL of A but, as we can see in Fig. 1.1, the two QWs are switched. Having three different structures will be important in order to understand the behaviour of this technology and the path to undertake for a reasonable modelization.

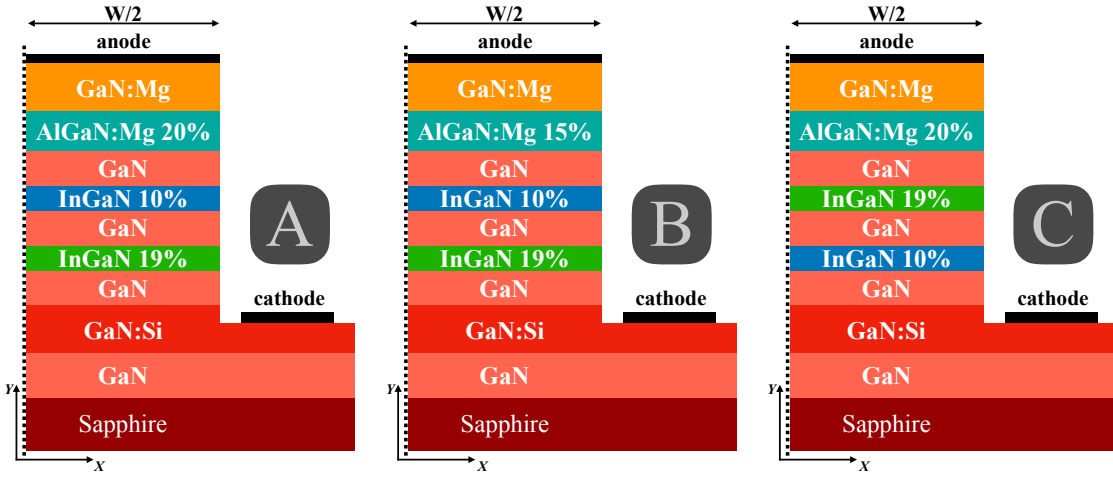


Figure 1.1: Cross section of each LED structure under study. Only one half of the structure is reported, thanks to the symmetry along the lateral direction \vec{x} . The symmetry axis at the center of each mesa is represented as a dotted line. The figure is not drawn to scale.

1.1.2 Experimental details

The set of experimental measurements received from the University of Padova contains an important amount of data that facilitate a deep understanding of the physical behaviour of the devices previously described. By repeating the same procedures of characterization on several devices with the same structure the set becomes more reliable, in other words, the variability of each wafer is taken into consideration. Accordingly, the characterization at room temperature has been performed on four samples for structure A, on three for both B and C, with the

addition of a fourth sample to the latter for the temperature dependence. However, two of the three samples measured for B show an evident shift in tension of the order of few volt in the IV characteristic. Therefore, to avoid an unjustified increase of the variance of the dataset, the two samples in question are not considered in the experimental analysis. Regardless, this situation allows us to understand the importance of redundancy during any experimental characterization.

The physical quantities measured are the IV characteristic and the EL spectrum (see Fig. 1.2 and 1.4). Here are reported the average values between the samples of each structure and the evaluation of the secondary physical quantities, as the total optical power and the external quantum efficiency, using directly the average values. In addition, a final L-I measure of structure C is performed to have a thick mesh in terms of current when evaluating the total optical power. This final quantity is measured as the voltage drop of a diode illuminated by the studied sample. All the measurements related to the optical power are not calibrated since it was not used an integrating sphere, as a matter of fact, only the light emitted from the top of the wafer is intercepted.

1.1.3 IV characteristics

In Fig. 1.2 the experimental IV characteristic of each structure is presented with the relative differential resistance. The voltage range is restricted to the quadrant related to the direct polarization to emphasize the working region of the LEDs. The differential resistance has been calculated using equation 1.1. A linear interpolation of the IV characteristic is mandatory in order to have a considerably smooth trend of the derivative. The fluctuation of the measures between each step of the experimental mesh is a common issue and it can lead to high values of the first derivative. Indeed, the mesh of the voltage axis is reduced by a factor 5.2. In this way it is possible to skip the current step in the IV characteristic right above 2 V and avoid the huge increment of the derivative.

$$R_d = \frac{\partial V}{\partial I} \tag{1.1}$$

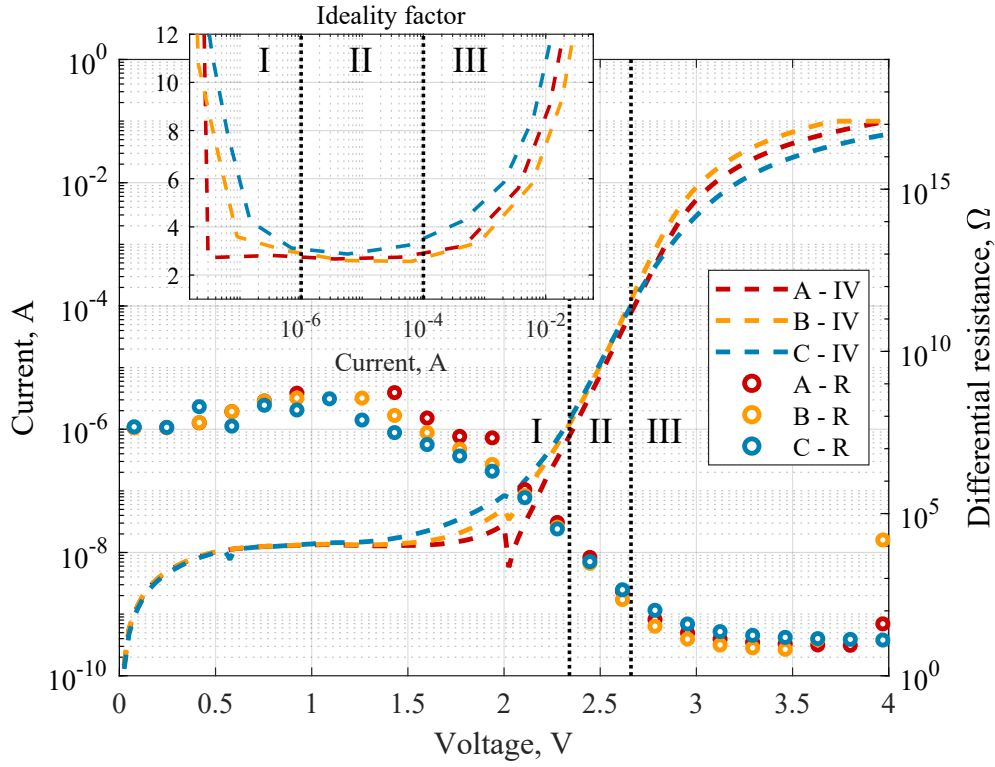


Figure 1.2: [T=298 K] Experimental IV characteristics (logarithmic scale) of the LEDs and differential resistances. The ideality factor is reported in the side plot (current in logarithmic scale).

This recurrent step, greater for structure A, is due to a switch of the full-scale range in the experimental equipment. Another important aspect of the adopted experimental procedure to mention is the saturation of the measures at 100 mA, which is the reason why the tensions greater than 4 V are not considered. However, there is no resulting lack of information for the working region below 4 V.

The ideality factor is evaluated for each structure as follows [5] [6]:

$$\eta = \frac{1}{V_T} \left[\frac{\partial(\log I)}{\partial V} \right]^{-1} \quad (1.2)$$

where $V_T = (k_B T)/q$. We can identify three different domains from the ideality factor with respect to the current in logarithmic scale. The I domain (below 1 μ A) indicates the existence of current-dependent parasitic shunt resistance in the LEDs. More precisely, the shunt resistance is caused by the manufacturing defects and, considering the circuit diagram of the device, is placed in parallel to the junction. A low value of the shunt resistance causes losses in both LEDs and

solar cells by providing an alternate current path for the current.

Instead, the III domain (above $100 \mu\text{A}$) is influenced by the series resistance and therefore is dependent on the current crowding effect. Actually, the higher increase of the ideality factor for the structure C suggests that its series resistance is higher in comparison to structure A and B. For this reason, the power conversion efficiency of structure C is compromised, because a fraction of the injected power is not converted in light radiation. This difference of the series resistance suggests that the current crowding effect is affected by the changes in the LED geometries.

In the II domain (between $1 \mu\text{A}$ and $100 \mu\text{A}$) the impact of the shunt resistance and the series resistance can be neglected and the IV characteristic follows an exponential trend. In all the three structures the ideality factor in the II domain does not go below a value of 2. For this reason we can say that all the three geometries are affected by current crowding as *Malyutenko et al.* [6] had verified in their experimental work.

1.1.4 Total optical power

The total optical power of the different structures is reported in Fig. 1.3 together with the IV characteristics. The computation of the total optical power is straightforward as shown in equation 1.3, where $I_{EL}(I, \lambda)$ is the electro-luminescence intensity spectrum and the integration limits used are selected from the experimental wavelength range: $\lambda_{min} = 178 \text{ nm}$, $\lambda_{max} = 891 \text{ nm}$.

$$P_{opt}(I) = \int_{\lambda_{min}}^{\lambda_{max}} I_{EL}(I, \lambda) d\lambda \quad (1.3)$$

The experimental EL spectra are given for a discreet set of current values: $20 \mu\text{A}$, $50 \mu\text{A}$, $100 \mu\text{A}$, $200 \mu\text{A}$, $500 \mu\text{A}$, 1 mA , 2 mA , 5 mA , 10 mA , 20 mA , 50 mA . As a consequence an interpolation of the IV characteristic data is mandatory to relate the current of each spectra to a certain voltage in order to sketch the total optical power with the IV characteristic. Even if the spectra are reported in arbitrary unit (see Fig. 1.4), they are still comparable and this comparison is inherited by any physical quantity related to them. That said, we can proceed comparing the total optical power of each structure. We can start appreciating a linear growth

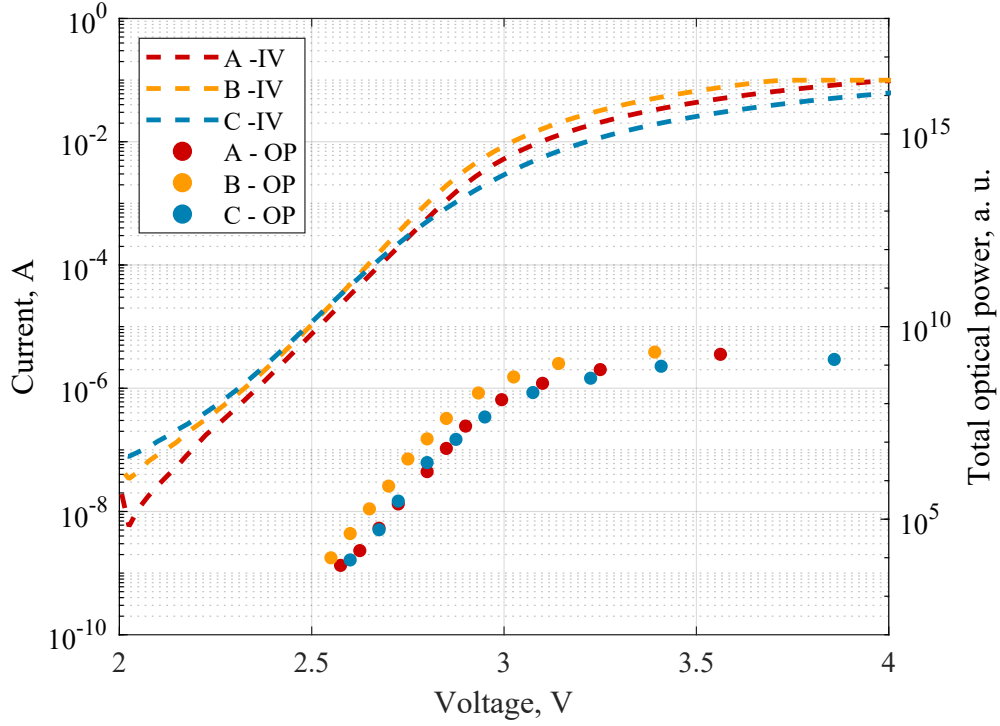


Figure 1.3: [T=298 K] Experimental IV characteristics (logarithmic scale) of the LEDs and total optical power in arbitrary unit.

Table 1.1: Values of the polarization at the beginning of the photo-luminescence, $20 \mu\text{A}$, and for the EL spectrum with highest current flow, 50 mA .

Structure	A	B	C
Bias at $20 \mu\text{A}$, V	2.57	2.55	2.6
Bias at 50 mA , V	3.56	3.39	3.86

that goes till 3 V, followed by a square root-like behaviour. All the curves reach saturation at a comparable value, except for structure C where the saturation occurs for a lower value caused by the fact that the EL spectra are completely missing the photo-luminescence peak related to one of the QWs. Further analysis will be performed with Fig. 1.4. Moreover, the saturation of the total optical power is reached for different values of bias, in table 1.1 the voltages reported for 50 mA have an important difference. A remarkable discrepancy in terms of efficiency is a direct consequence of this voltage variation with fixed current. In our case, structure C requires the highest voltage to reach 50 mA, meaning that its efficiency will be compromised.

1.1.5 Electro-luminescence spectrum

In Fig. 1.4 we can find the EL spectra, representations of the spontaneous LED light emission resolved in wavelength. In order to simplify the representation, we have reported only the mean value and therefore we can appreciate a smooth trend of the measures. A roughening process on the light-emitting surface of the device was not performed by the designer to eliminate the Fabry-Perot interference oscillations. The fringes are caused by the cavity formed by the GaN/air interface and the sapphire/GaN interface which form the two reflectors of the cavity [7] [8]. The difference in the refractive index on the top flat surface between the gallium nitride and the air leads to a certain reflectivity of the light emitted by the active region inside the device, therefore the efficiency of the LEDs is affected. On the contrary this phenomenon vanishes with a textured surface.

As the current injection increases, a blue-shift of the peak maxima can be recognized in the three structures. To be more specific, the shape of the spectrum is dependent on the variation of the energy transitions of the carriers in the QWs. With high injection the contribute of energy transitions between secondary confined states increases because the fundamental confined states are already saturated. The energy step between the secondary states is higher, meaning that the wavelength of the emitted photons is shorter, causing the blue-shift.

Moreover the different magnitude of the peak related to the blue QW makes it simple to understand the effect of the EBL. If we look at the EL intensity of structure C, where the blue QW is no more near the EBL, the blue peak disappears. This experimental evidence suggests that the design of an active region with MQW should have the QWs with lower In molar fraction near the EBL. Actually, the small hole mobility in GaN-based devices makes improbable to have a homogeneous hole concentration in the active region, besides the holes have a high probability to be captured by the first QW, counting from the p-side of the device.

1.1.6 External quantum efficiency

When characterizing any electronic device, the evaluation of the efficiency as a function of the injected current or of the temperature is mandatory. We can define

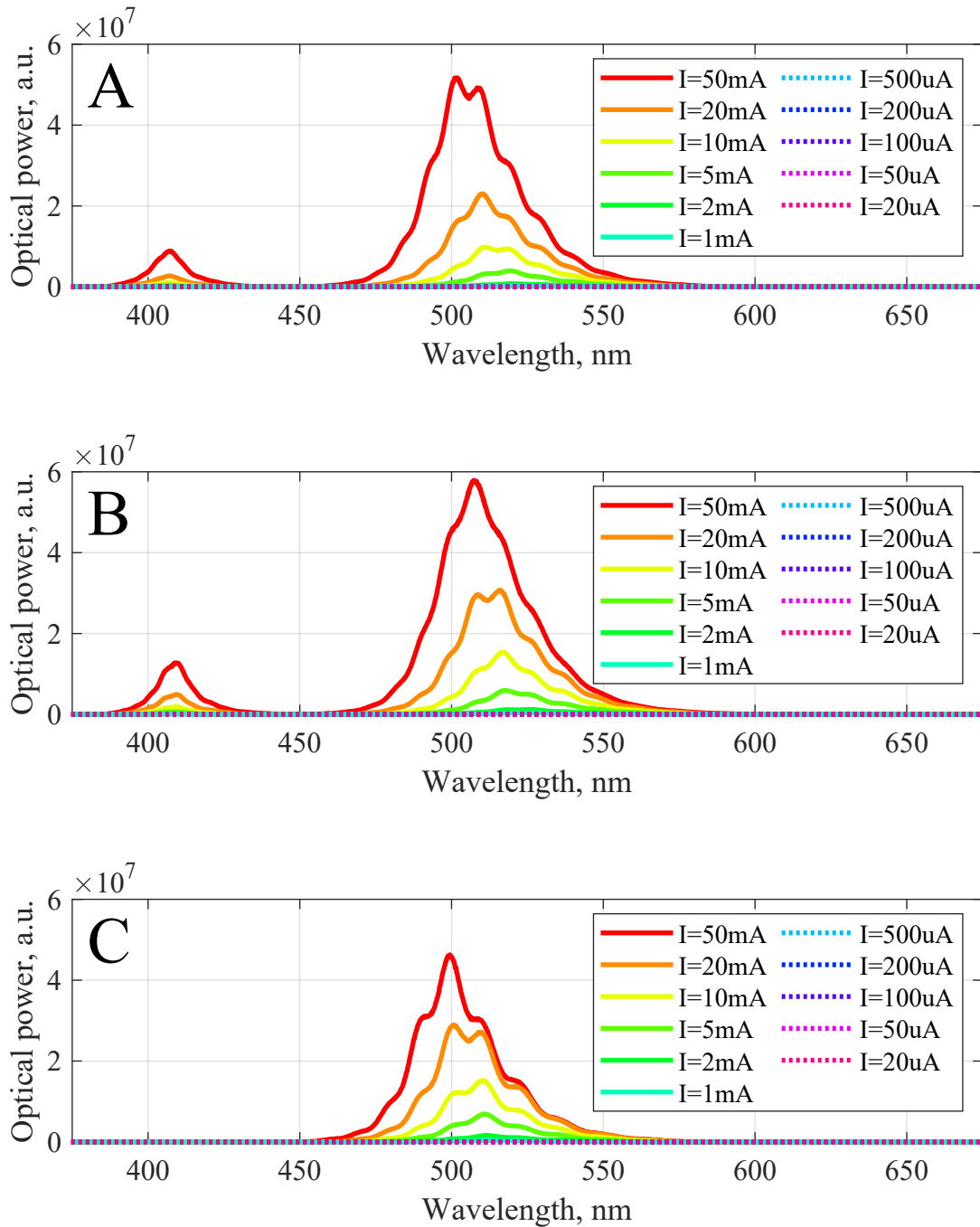


Figure 1.4: [T=298 K] Experimental EL spectra given for a discrete set of current values: 20 μ A, 50 μ A, 100 μ A, 200 μ A, 500 μ A, 1 mA, 2 mA, 5 mA, 10 mA, 20 mA, 50 mA. The intensities are in arbitrary units.

two different types of efficiency that are dependent on each other: the internal quantum efficiency (IQE) and the external quantum efficiency (EQE). The former is defined as the ratio between the number of photons emitted internally for the number of carriers passing the junction. In other words, it can be seen as the ratio of radiative recombination for the total recombination rate. Here follows the equation:

$$IQE = \frac{R_r}{R_r + R_{nr}} = \frac{Bn^2}{An + Bn^2 + Cn^3} \quad (1.4)$$

where n is the electron concentration and A , B and C are the Shockley-Read-hall (SRH), radiative and Auger recombination coefficients, respectively. As we can see, the expressions of the recombination rates are given by the ABC model (see appendix B.3 for more details). The EQE is the ratio between the number of photons emitted externally for the number of carriers passing the junction, meaning that the correlation with the IQE is straight-forward. From the equation 1.5 we see that the only difference is the consideration of the photon extraction efficiency EXE, also called optical efficiency.

$$EQE = EXE \times IQE \quad (1.5)$$

The EXE takes into account the light refraction at the semiconductor/air interface. The Snell's law defines a certain critical angle for which the light is completely reflected at the interface as a consequence of the variation in the refractive index. In our case, the EXE cannot be neglected because a roughening process on the light-emitting surface of the device has not been performed on the three LED structures, as previously announced. However, the EXE decreases the absolute value of the EQE with the same amount in the whole current injection range because it has a dependence on the wavelength of the emitted light and not on the intensity. Following this tendency, the normalized trend of the EQE and the IQE as a function of the current are comparable [9].

The computation of the experimental EQE (see equation 1.6) is always carried out for the values of currents of the measured EL spectra. P_{IV} is the product between each current step and the interpolated tension from the IV characteristic. The EQE is presented in Fig. 1.5 with the total optical power, both with respect to

the current and not normalized.

$$EQE = \frac{P_{opt}(I)}{P_{IV}} \quad (1.6)$$

The trend of the EQE and the total optical power are cutted below 2 mA to zoom in on the current range where the drop in efficiency appears and to avoid the low injection region where the behaviour is highly affected by the noise. If we do not consider the magnitude of the EQE of each structure, we can notice a similitary between the trend of structure A and B, whereas the one of C seems to be shifted at lower currents. Now, considering the differences between the three geometries,

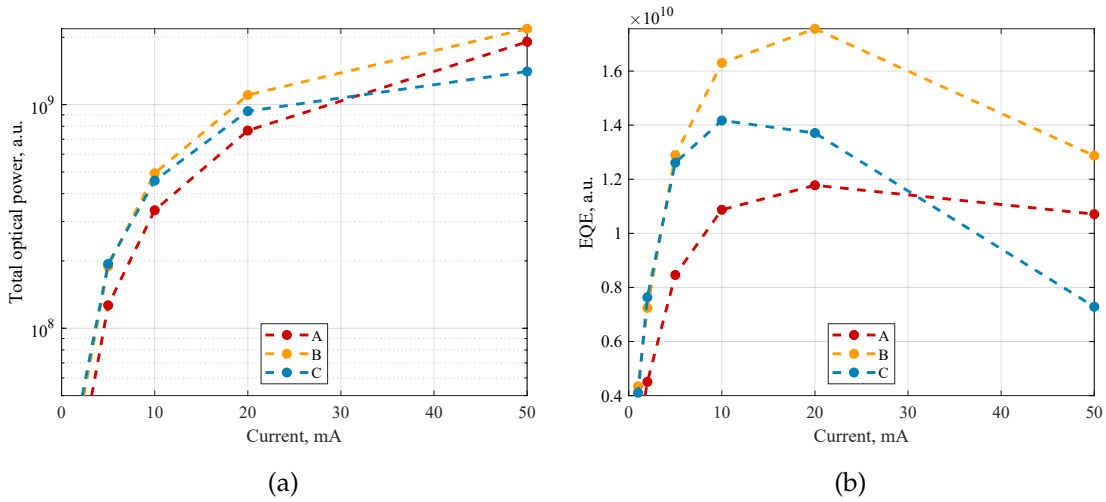


Figure 1.5: [T=298 K] (a) Total optical power in arbitrary unit (logarithmic scale). (b) EQE in arbitrary unit.

the evaluation made above fits perfectly. Structures A and B are slightly different one from each other while structure C has the QWs in the opposite positions. Coming back to the absolute values, the EQE starts to decrease from 20 mA: this phenomenon is called efficiency droop. While, at low injection, the efficiency of structure A grows slowly with respect to structure B. This evident difference in the efficiency trend should be associated to the Al molar fraction of the EBL, which is 0.2 for structure A and 0.15 for B.

1.2 Simulation analysis

The first section of this part is entirely dedicated to the description of the adopted geometry and of the essential parameters in order to perform a satisfactory simulation. In the second section the simulations are compared with the experimental measurements. Only the results related to the reference structure A are exploited in order to avoid redundancy. However, similar outcomes have been verified for structure B and C. The analysis involves an initial interpretation of the band diagram and the carrier concentrations, then the fit of the IV characteristic and the EL intensity is verified. In conclusion a comparison between the total optical power and the efficiency is depicted using the L-I measurements of structure C.

1.2.1 1D modelization and simulation parameters library

The 1D simulations of the 3 structures have been performed using an approximated version of the real geometries. In Fig. 1.6 is represented the 1D model of the structure A. It appears in a column-like shape since the simulator requires at least two mesh points on the direction \vec{x} , giving to the geometry a certain width fixed to $500 \mu\text{m}$ as in the real device. For the simulation is considered only the

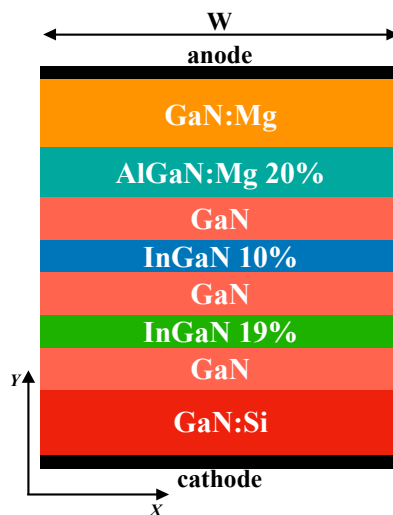


Figure 1.6: Simulated 1D geometry of structure A. The apparent width of the column-shaped device along the \vec{x} direction is fixed to $500 \mu\text{m}$. The figure is not drawn to scale.

top working part of the global mesa structure, while the sapphire substrate, the

Table 1.2: Main parameters of the quantum corrected DD simulations.

T, K	298
$\nabla T, \text{Kcm}^{-1}$	Not considered
Statistics	Fermi
Ionization	Incomplete
Quantum	on
$x_{pol}, \text{norm.}$	0.4
τ_{scat}, s	5×10^{-14}
τ_{SRH}, s	9×10^{-7}
$B, \text{cm}^3\text{s}^{-1}$	2×10^{-11}
$C, \text{cm}^6\text{s}^{-1}$	2.7×10^{-30}
Δ_{wave}, nm	5
E_{tail}, meV	80
O_{ff}, meV	670
E_A, meV	200
E_D, meV	20

undoped GaN layer and part of the n -type GaN are removed. Therefore, below a 100 nm thick n -type GaN is directly placed the cathode. The final implemented geometry is far from being a realistic representation of the real LED. In fact the presence of the cathode located only on the side of the mesa structure and the effect of the edges could be taken into consideration exclusively in a 3D simulation, more time consuming but less efficient in terms of final results.

In table 1.2 are reported the parameters of the simulation. The temperature is fixed at 298 K since the first set of experimental data was taken at room temperature. Nonetheless no thermal conduction is considered by the simulations, in other words the temperature is constant in all the simulated device.

[Quantum=on] stands for the application of the quantum corrections to the DD model. A self-consistent model is used to evaluate the confined states inside the QWs. This method becomes mandatory when considering polarization charges as in the case of InGaN/GaN structures, where the QW is tilted to one-side. The self-consistent carrier density model is summarized in appendix B.2.

Remaining on this topic, the wave-range parameter Δ_{wave} defines the left and right limit where the confined wave-function is solved; the selection of this parameters depends on the thickness of the QWs and of the barriers.

For what concerns the intrinsic polarization of the material (see appendix A.1.1 for more details), the fraction of their effect is fixed at the reasonable value of 0.4, their huge impact on the IV characteristic and on the efficiency of the device will be analyzed later.

The scattering time is a parameter defining the gain broadening due to carrier scattering depicted by the Landsberg model. It also directly affects the shape and magnitude of the spontaneous emission spectrum of the LED.

The SRH lifetime, the radiative and Auger recombination coefficients are the parameters related to the standard ABC model where the final recombination rate is given by:

$$R = R_{spont} + R_{aug} + \frac{n}{\tau_n} + \frac{p}{\tau_p} \quad (1.7)$$

the values are taken from a study performed on LEDs without EBL technology, *Calciati et al.* [10]. For more details see appendix B.3.1, B.3.2, B.3.3.

The parameter E_{tail} in equation 1.8 describes an exponential tail of the joint density of states into the energy gap. Here follows a formulation of the JDOS near the energy gap:

$$JDOS = \rho_r e^{\left[\frac{E-E_{edge}}{E_{tail}}\right]} \quad (1.8)$$

where E_{edge} is the energy of the band edge and ρ_r is the reduced density of states.

The band offset O_{ff} is normally defined as follows:

$$O_{ff} = \frac{\Delta E_c}{\Delta E_c + \Delta E_v} \quad (1.9)$$

however in the presence of strain, the model uses the highest valence band because of the splitting between HH and LH bands [11].

The final parameters are the activation energy of acceptor and donor E_A and E_D . In addition, in table B.2 are provided the parameters useful to replicate the simulations.

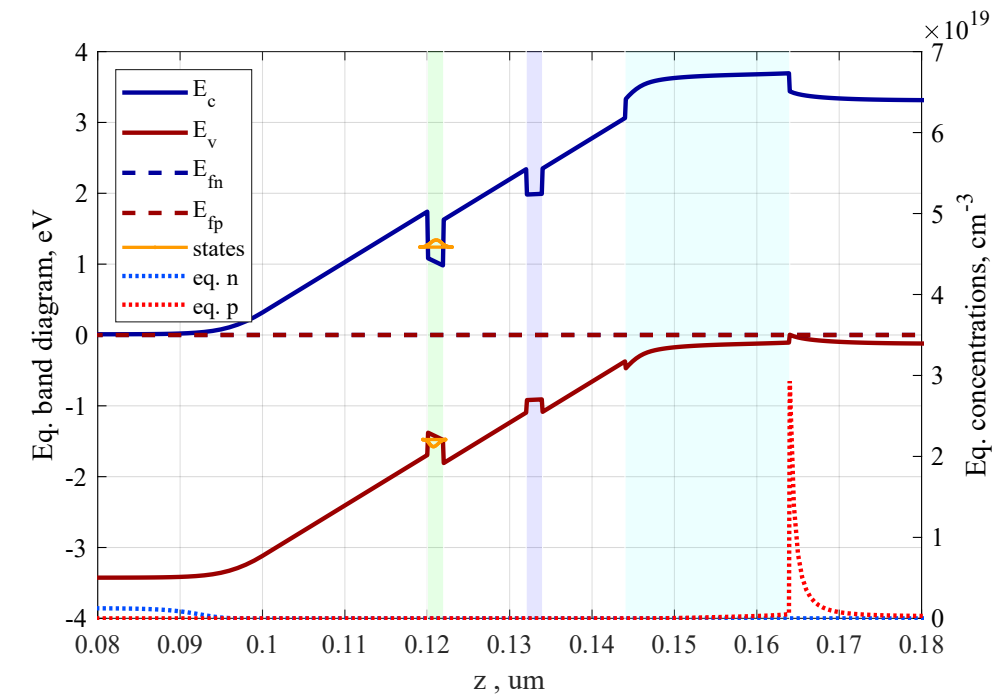
1.2.2 Simulation results

Band diagram and carrier concentrations

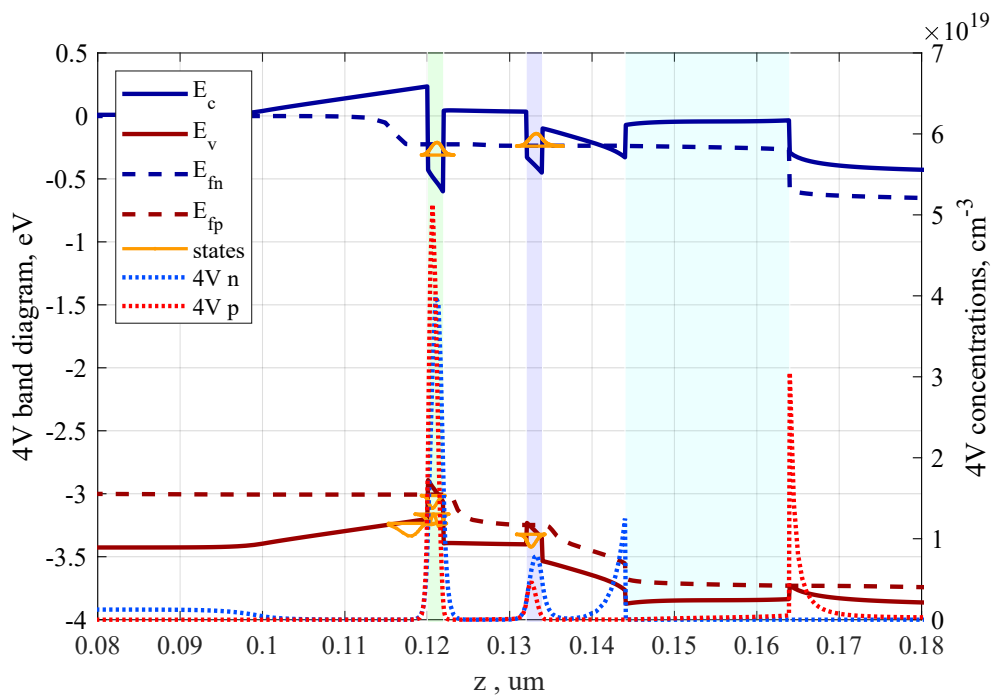
We can start focusing on the band diagram, see Fig. 1.7 where a magnification over the active region is reported. As expected more confined states are found at high bias. Even if it is not visible from the figure, the fundamental confined states in the blue QW appears just above 3.5 V, having consequences on the emission efficiency of that particular well. On the contrary for the green QW the fundamental confined states in conduction and valence band are established from the equilibrium condition, as a consequence of the In molar fraction higher value, which leads to an easier confinement. At a tension of 4 V the carriers are mainly located inside the two wells, however we can appreciate an important electron concentration on the left of the EBL and a hole concentration on the right. The electron concentration on the left represents the correct working process of the EBL, without it there would be a too small electron concentration in the blue QW that would hinder a sufficient np product for a reasonable light emission of the well. Instead, the hole concentration on the right, also related to the effect of the interface with the EBL that generates a step on the valence band, is a consequence of the small value of the hole mobility (see table B.2).

Furthermore, a comparison between the carrier concentrations at 4 V for all the three LED structures is presented in Fig. 1.8. When looking at these figures we must remember that in structure C the QWs are switched. The main difference appears in the electron concentrations inside the blue QW, for this reason the exact values are reported: $n_A = 7.9 \times 10^{18} \text{ cm}^{-3}$, $n_B = 9 \times 10^{18} \text{ cm}^{-3}$, $n_C = 3.3 \times 10^{18} \text{ cm}^{-3}$. We can notice that having the blue QW near the EBL is the best choice, moreover the electron concentration in the green QW is not affected by the QW relative position. For these reasons, the structure B has the best design when maximizing the carrier injection in the active region.

Besides, no hole blocking layer (HBL) is present in the three designs. Its effect on the hole concentration profile would be minimal because of the small fraction of carriers that can reach the n-side of the active region. Also the electron concentration flowing from the n-side into the active region would get smaller.



(a)



(b)

Figure 1.7: (a) Band diagram of structure A at equilibrium with confined states of the QWs and carrier concentrations. The QWs and the EBL are highlighted with light colors, the colors of the QWs are related to their optical emission. (b) Band diagram of structure A at 4 V, figure depicted as the one at equilibrium.

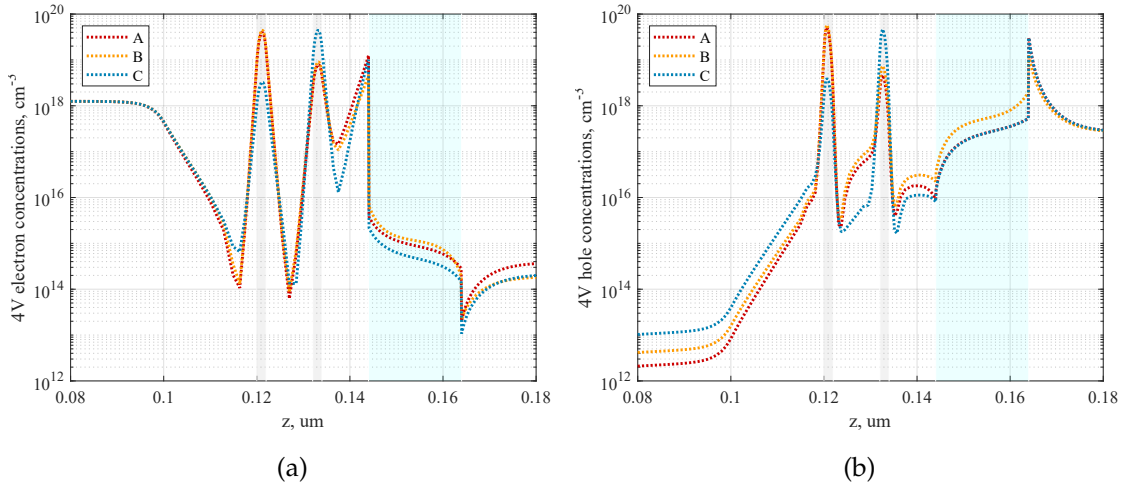


Figure 1.8: (a) Comparison of the electron concentrations at 4 V in the three LED structures. The two QWs are highlighted in light gray and the EBL in light blue. (b) Comparison of the hole concentrations; figure depicted as (a).

IV characteristic

In Fig. 1.9 the experimental IV characteristic is compared with the one simulated in the range between 2 V and 4 V. As announced before, the effect of the polarization charges on the IV characteristic is strong. Almost one order of magnitude in terms of current, at fixed bias 3 V, with a change of 0.2 in the fraction of the intrinsic polarization is appreciable. A convenient agreement in the middle range of the IV, the part related to the light emission, can be reached with a fraction of polarization charges equal to 0.6. However, the simulations start to increase above 3.3 V reaching a final buildup of almost two order of magnitude in terms of current at 4 V. This misleading shape must be associated with a lack of resistivity behaviour of the simulated structure. We are here referring to the absence of the undoped GaN buffer layer, the $1.4 \mu\text{m}$ section of n doped GaN and the contact resistance. This phenomenon can be simulated by applying a virtual series resistance to the simulated device, the resulting IV will have saturation for high bias following the experimental trend. Nonetheless the effect of the current crowding increases with the bias and therefore the section of the LED in which there is an effective charge flow is smaller bringing to an increase of the resistance. We have to remember though that the current crowding is not considered by the 1D simulated geometry, leaving so another grade of freedom on the IV at high bias.

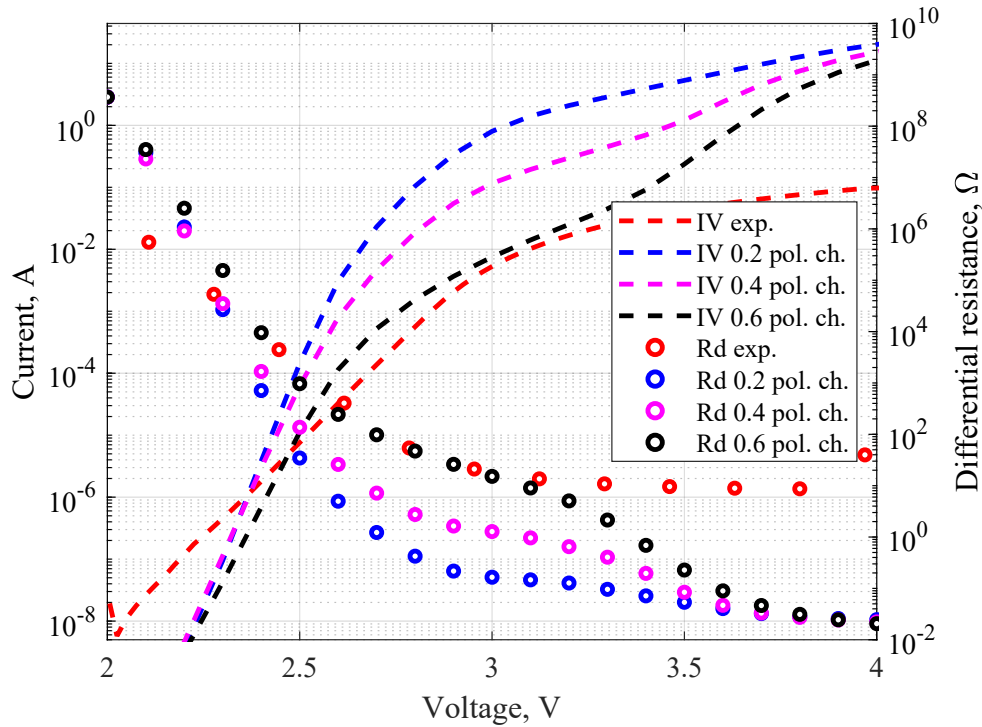


Figure 1.9: IV characteristic curve and differential resistance of structure A (logarithmic scale). Comparison with the experimental results and the dependence of the fraction of polarization charges are presented. The simulator reports the IV characteristic in Am^{-1} , multiplying by W we obtain the curve in figure.

Spontaneous emission spectrum

We can now move on to the light emission performances of the device. Instead of going straightforward in the spontaneous emission spectra, a theoretical regression is helpful to understand better the final results we obtained. The emission wavelength of each well is directly related to the energy gap and since the quantum confinement takes place between the GaN barriers, the photon emission is more precisely related to the energy gap between the two fundamental confined states in the conduction and valence band, which we will call the effective energy gap E_{eff} (see equation 1.10). In appendix A (Fig. A.4) is reported the dependence of the nominal energy gap E_{nom} of the bulk InGa_N alloy with respect to the In molar fraction and it is also given the related wavelength. From Fig. A.4 we can also notice that the two nominal energy gaps of the wells have been extracted

Table 1.3: Nominal energy gap and relative wavelength extracted from the dependence on the In molar fraction in Fig. A.4.

QW	E_{nom} , eV	λ_{nom} , nm
Blue	2.90	427.3
Green	2.46	503.5

together with the wavelengths; the values of which are presented in table 1.3.

$$E_{eff} = E_{nom} + E_1^e + E_1^h = \frac{hc}{\lambda_{eff}} \quad (1.10)$$

We can now start to look at the first comparison between the experimental spectrum at 50 mA and the simulated one at 4 V (Fig. 1.10.a). The experimental bias is selected to have high carrier injection in the wells and to stay drastically away from the noise level, as we can see in the measurement at low current. Instead, the bias of the simulated spectrum has been chosen high because, as previously said, there are no confined states for lower voltages, which is further observable from the low radiative recombination in the blue QW (Fig. 1.10.b). However, the match of the polarizations is not relevant for our kind of study, because the experimental spectra are in arbitrary units and therefore, we are only looking at the position of the peaks in terms of wavelength in a normalized figure.

As a connection between the theory and the plotted data, the nominal and effective wavelengths of the wells are sketched as vertical lines. The actual reasons of this highlight are the perfect superposition of the peaks of the simulated spectrum with the effective wavelength and the interesting fitting of the nominal wavelength of the green QW with the experimental peak. The first consideration could be seen as a verification of the simulation quality. While the last remark suggests a probable difference in the relation of the InGaN energy gap with reference to the In molar fraction between the bowing equation A.6, used for our simulations, and the method of the device manufacturer. In addition, also the selection of the working devices during the production process could represent a cause of this discrepancy. This choice depends on the emission wavelength, which is required at 505 nm for the green QW and does not consider a verification of the composition in the wells. However, the mismatch between the peaks

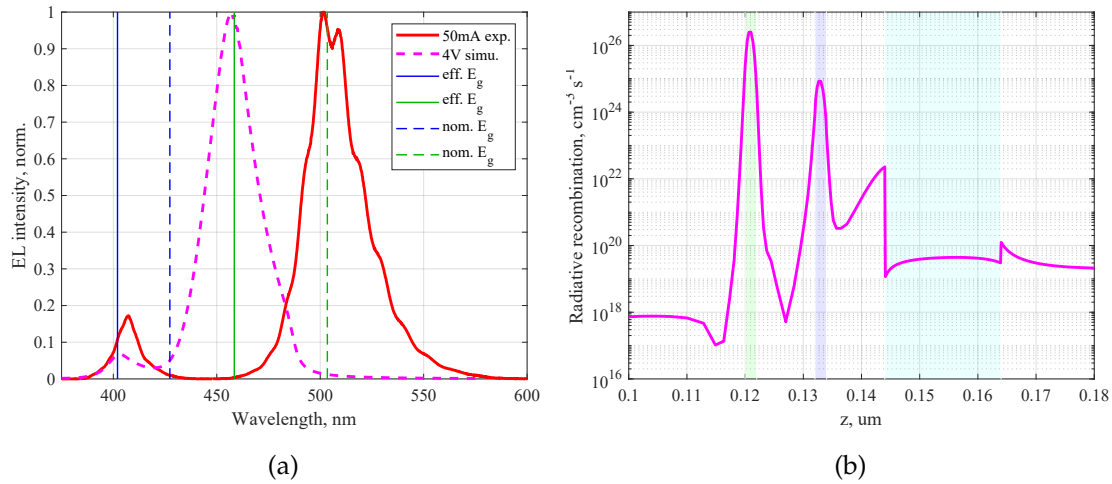


Figure 1.10: (a) Comparison of the EL intensities: experimental at 50 mA, simulated at 4 V. The vertical lines select the wavelengths related to the nominal and effective energy gaps. (b) Radiative recombination spatially resolved.

of the green well is equal to 46 nm and cannot be associated just with the reasons described above. Therefore in the next step we will summarize the important dependences of the spontaneous emission spectrum (see Fig. 1.11, 1.12).

Guided wavelength shift of the spectrum

The first variable we are going to change is the In molar fraction of the QWs (see Fig. 1.11.a) to a value of ± 0.01 that is also the error inside the green QW given by the manufacturer. As a consequence of this wavelength shift, we can generate an overlapping curve by simply changing the In molar fraction, to 0.11 for the blue QW and to 0.25 for the green one. This overlap is reported to create an idea of the dependence, but we have to keep in mind that the composition fluctuations of In in the direction longitudinal with respect to the wells is an established issue for III-N hetero-structures [12]. The In atoms inside the wells tend to form clusters defining a longitudinal trend of the InGaN composition [13]. For this reason atomistic simulations have been applied to GaN-based LEDs [14]. If we consider also the effect of the current crowding, there is the possibility of having high carrier injection only in the section of the well that has incorrect In molar fraction as a consequence of the fluctuations. Therefore, a 2D simulation should be performed to take control of the composition in the longitudinal direction.

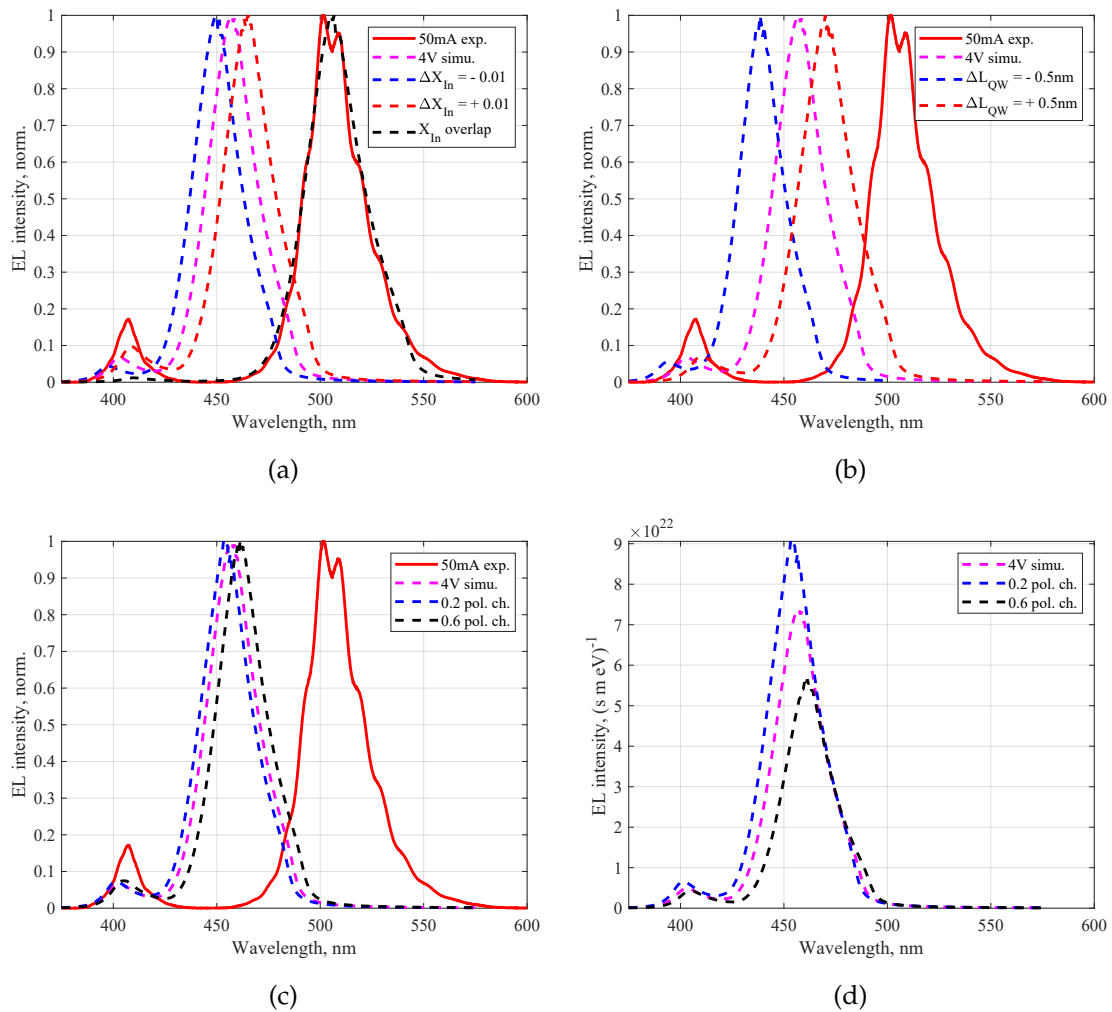


Figure 1.11: (a) Normalized EL intensity, dependence on the In molar fraction inside the QWs. Overlap with 0.11 for the blue QW and 0.25 for the green QW. (b) Normalized EL intensity, dependence on the thickness of the QWs. (c) Normalized EL intensity, dependence on the fraction of polarization charges. (d) Not normalized EL intensity, dependence on the fraction of polarization charges.

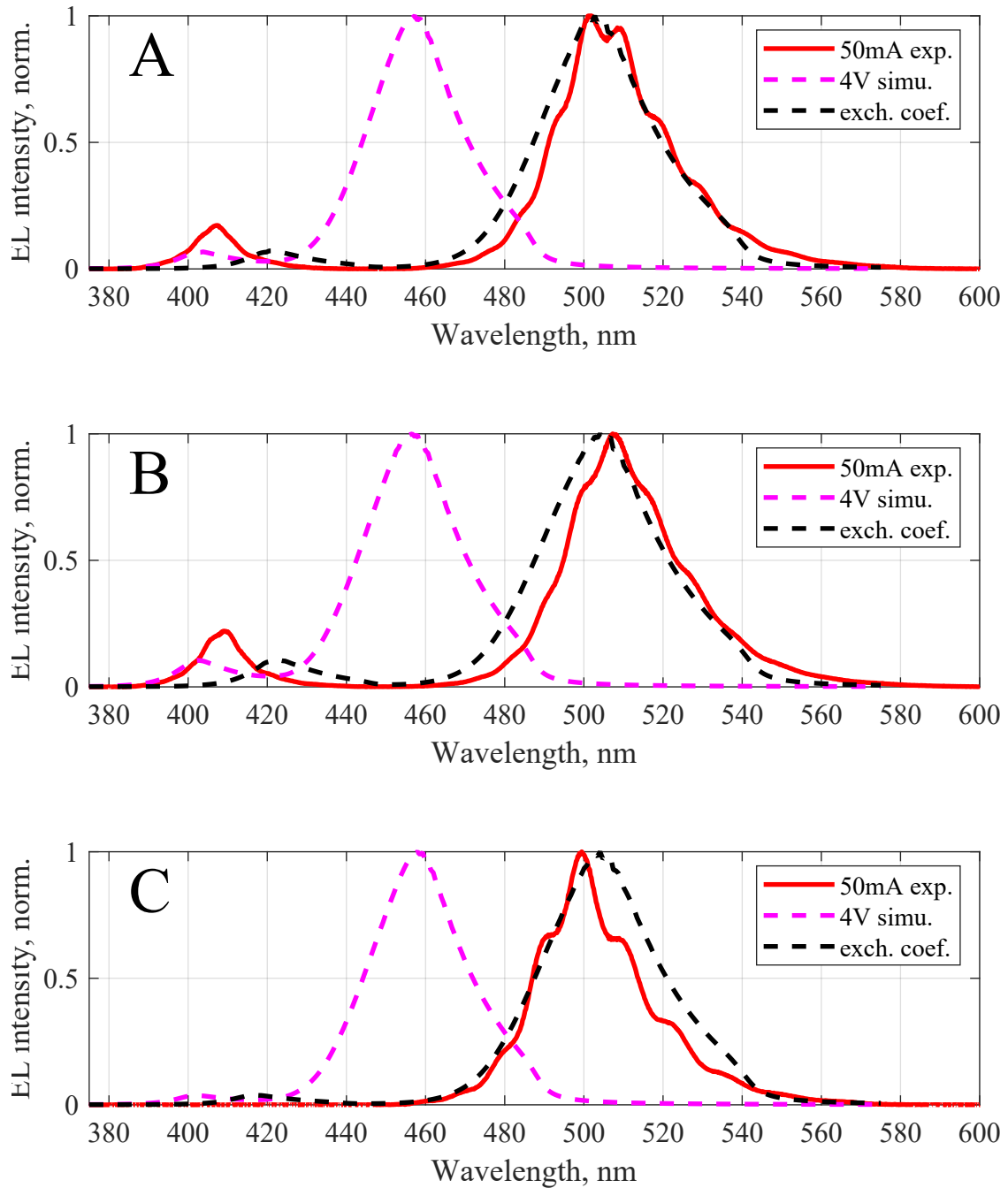


Figure 1.12: Effect of the coulombian interactions on the EL spectrum of structure A, B and C. The exchange coefficient has been applied with a value of 8×10^{-8} eVcm for all the three structures.

The next variable analyzed is the thickness of the wells (see Fig. 1.11.b). With a variation of $\pm 5 \text{ \AA}$ the shift in terms of wavelength is evident thanks to the inverse proportionality of the confined state energy with respect to the thickness of the well, reported in equation 1.11 in the infinite well approximation, where L is the QW thickness and $m_{e|h}$ is the electron or hole effective mass.

$$E_1^{e|h} = \frac{h^2}{8m_{e|h}L^2} \quad (1.11)$$

However, this dependence disappears as the thickness is increased, since given that the quantum confinement is no more possible in the large well and the emission peak decreases. Reason why an overlapping curve is not reported in this case.

The fraction of polarization charges has an important effect on the spontaneous emission spectrum (see Fig. 1.11.c). The small horizontal shift must be associated with an important decrease of the peaks as the polarization charges increase, leading to an efficiency drop of the LED. In order to understand the effect that the polarization charges have on the absolute value of the intrinsic polarization, the same EL intensities are presented in absolute value (see Fig. 1.11.d). The given unit of magnitude finds an explanation in appendix B.3.2.

A not reported dependence investigated concerns the thickness of the undoped GaN barrier between the QWs, because a realistic variation of $\pm 3 \text{ nm}$ does not affect the EL spectrum.

The last investigated dependence of the EL intensity spectrum is the effect of the many-body renormalization model. Briefly, we can say that in deep InGaN/GaN QWs the small energy gap leads to coulombic interactions between the two carrier species. The many-body attractive force within the concentrations in the well is modelled with the renormalization of the energy gap, meaning that the gap is reduced by a certain ΔE . Different models have been developed to reproduce the renormalization effect. In this work an empirical approach has been selected given the fact that the final energy shift would be equal to the theoretical model. Furthermore, a theoretical approach requires an higher number of parameters that would make the simulation complex and unmanageable. The model is

shown in equation 1.12,

$$\Delta E_g = A_x \left(\frac{n+p}{2} \right)^{\frac{1}{3}} \quad (1.12)$$

where A_x is the empirical parameter governing the energy shift, called exchange coefficient and measured in [eVcm], n and p are the electron and the hole concentrations in the well. In Fig. 1.12 the exchange coefficient is equal to 8×10^{-8} eVcm so that we can have superposition between the spectra. It is important to underline the reproducibility of the superposition for all the three LED structures which have same value of exchange coefficient. However this empirical model is

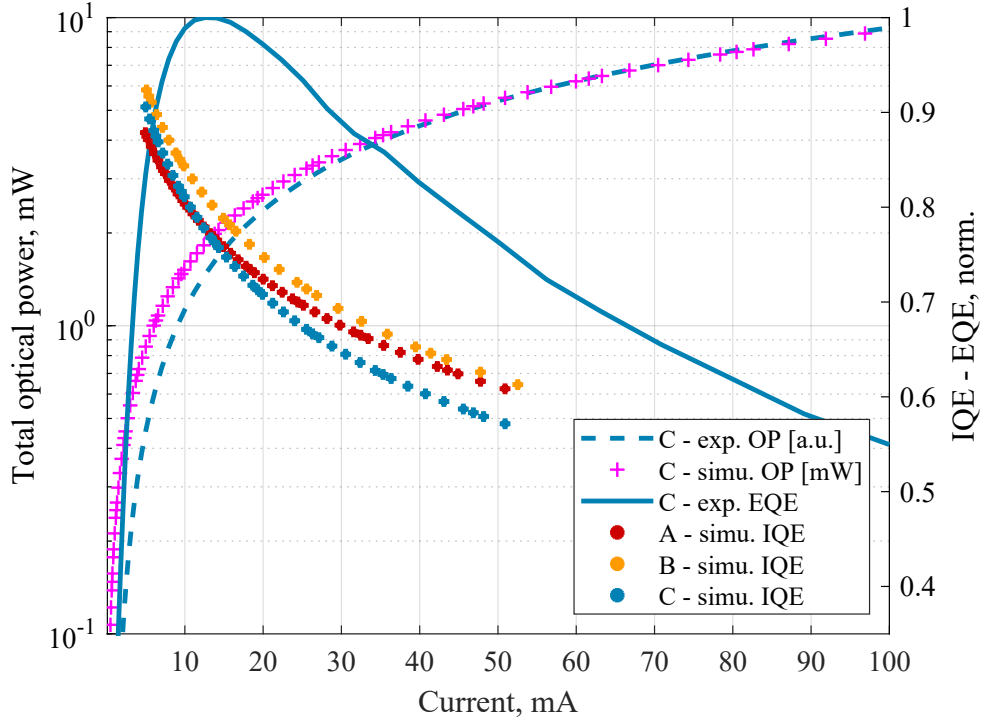


Figure 1.13: Experimental total optical power and EQE of structure C as a function of the current injection. Simulated internal optical power of structure C and simulated IQEs of the three structures with $x_{pol} = 0.6$.

not applied with a different magnitude for each QW, in fact a smaller renormalization would be expected for the blue QW with a bigger energy gap.

Efficiency droop

In Fig. 1.13 the L-I measurements of the integrated optical power performed only for structure C are reported in arbitrary units. The experimental EQE is evaluated

by means of equation 1.6. The experimental total optical power is normalized by a factor in order to have superposition with the simulation at 100 mA and to verify the correct trend of the simulated internal optical power. As said before, it is possible to compare the internal and external physical quantities because the EXE has a slightly constant dependence with respect to the current injection. Moreover, x_{pol} has been fixed to the value of 0.6 in order to fit the experimental characteristic, as shown in Fig. 1.9.

The trend of the simulated efficiencies has been reported only for the relevant range of current injection. We can notice the typical decrease for high injection currents caused by the growing magnitude of the Auger recombination, that has actually been prove to be the main reason of the efficiency droop [15]. Nonetheless, the increase of the Auger coefficient causes the increase in absolute value of the negative curve slope; the chosen value replicates correctly the experimental slope. As a final consideration, the relative trend between the three structure is completely coherent with the experimental EQEs (see Fig. 1.13.b).

InGaN/GaN LED temperature behaviour

2.1 Introduction

An high efficiency is a mandatory requirement in all the areas of application for GaN-based LEDs. The scientific community has particularly focused on the the efficiency droop, the mechanism for which the decrease of the IQE is due to high current density. Anyhow also the increase of the working temperature leads to an important limitation of the efficiency, a phenomenon that takes the name of thermal droop. Therefore, a deep walk-through in the temperature behaviour of the structure C is performed with the analysis of the IV characteristics in the temperature range 120-320 K and of the EL intensities in the range 120-350 K. In addition, a selection of thermal dependences is reported in order to give a complete view into the mechanisms, determining the temperature behaviour when simulating the LED.

2.2 Selection of thermal dependences

In table 2.1 a summary of the simulation parameters that have a historically recognized dependence in temperature is reported. Just the relevant dependences are included in the model since one of the main purposes is to keep the simulation simple and efficient.

Table 2.1: Modelization of thermal dependences of the main parameters used for the simulation at room temperature. It is recommended to read the section to understand the table.

$E_g(T) = E_g _{0K} - \frac{\alpha T^2}{T+\beta}$	[16]
$a(T), \text{Å}$	[17] [18]
$c(T), \text{Å}$	[17] [18]
$x_{pol}(T)$	Fig. 2.2
$O_{ff}(T) = O_{ff} _{300K} - [1 - O_{ff} _{300K}] \frac{\partial E_{gb}(T) - \partial E_{gw}(T)}{E_{gb} _{300K} - E_{gw} _{300K}}$	Eq. 2.1
$\mu_{n p}(T) = \mu_{n p} _{300K} \left[\frac{300}{T} \right]^{\alpha_{n p}}$	[19]
$R_c(T)$	Fig. 2.2
$\tau_{n p}(T) = \tau_{n p} _{300K} \left[\frac{300}{T} \right]^{\beta_{n p}}$	[19] [20] [21] [22]
$B(T) = B _{300K} \left[\frac{300}{T} \right]^\gamma$	[23] [19] [24] [21] [15]
$C(T) = C _{300K} \left[\frac{T}{300} \right]$	[25]
$E_A(T)$	[26]
$E_D(T)$	[26]

The temperature behaviour of the energy gap is given by the Varshni model [16], see equation A.5 and table B.2 for the parameters $E_g|_{0K}$, α and β of the model. The Varshni equation is a mandatory upgrade for a simulation in temperature since the magnitude of the energy gap is the key of micro-electronic devices.

For the lattice structure, the mean coefficient of thermal expansion for the a direction is determined to be $5.59 \times 10^{-6} \text{ÅK}^{-1}$ for the entire range from 300 K to 900 K, while for the c direction values of $3.17 \times 10^{-6} \text{ÅK}^{-1}$ and $7.75 \times 10^{-6} \text{ÅK}^{-1}$ are approximated for the temperature range 300-700 K and 700-900 K, respectively [17]. Going to smaller temperatures a mean expansion of $7.21 \times 10^{-6} \text{ÅK}^{-1}$ for a and $8.68 \times 10^{-6} \text{ÅK}^{-1}$ for c has been measured in the range 40-295 K [18]. The

polarization charge related to the wurtzite structure and the lattice mismatch and the interfaces is affected by the variation of the lattice parameters, however the strain due to the interfaces between the layers with different composition is strictly related to the considered device consequently to its temperature behaviour. The singularity of the phenomenon leads to a lack in the literature of the variation of polarization charge with respect to the temperature. Therefore the variation of intrinsic polarization is applied by manually varying the fraction of charges $x_{pol}(T)$ at the same time as the simulation temperature is changed.

As said before, the contact resistance $R_c(T)$ can be modelled in the simulation with an independent resistor placed in series on one of the two contacts. This important feature permits the fitting of the IV at high bias and the possibility to find the trend of the contact resistance with respect to the temperature.

The band offset $O_{ff}(T)$ has a thermal behaviour defined by the energy gap. In equation 2.1 the connection is reported from the fifth passage, while a first degree expansion is applied from the seventh passage having $(\partial E_{gb}(T) - \partial E_{gw}(T)) \approx 0$. The evaluation is reported for completeness, where E_{cb} , E_{cw} , E_{vb} and E_{vw} are the conduction and valence band energy levels of the barrier and the well, while E_{gb} and E_{gw} are the energy gaps of the barrier and the well; but the band offset is kept fixed in the simulation (see table B.2).

$$\begin{aligned}
 O_{ff} &= \frac{E_{cb} - E_{cw}}{E_{gb} - E_{gw}} = \frac{(E_{gb} - E_{gw}) - (E_{vw} - E_{vb})}{E_{gb} - E_{gw}} = 1 - \frac{E_{vw} - E_{vb}}{E_{gb} - E_{gw}} = \\
 &= 1 - \frac{E_{vw} - E_{vb}}{(E_{gb}|_{300K} - \partial E_{gb}(T)) - (E_{gw}|_{300K} - \partial E_{gw}(T))} = \\
 &= 1 - \frac{E_{vw} - E_{vb}}{(E_{gb}|_{300K} - E_{gw}|_{300K}) - (\partial E_{gb}(T) - \partial E_{gw}(T))} = \\
 &= 1 - \frac{E_{vw} - E_{vb}}{(E_{gb}|_{300K} - E_{gw}|_{300K}) \left(1 - \frac{\partial E_{gb}(T) - \partial E_{gw}(T)}{E_{gb}|_{300K} - E_{gw}|_{300K}}\right)} \approx \\
 &\approx 1 - \frac{E_{vw} - E_{vb}}{E_{gb}|_{300K} - E_{gw}|_{300K}} \left(1 + \frac{\partial E_{gb}(T) - \partial E_{gw}(T)}{E_{gb}|_{300K} - E_{gw}|_{300K}}\right) = \\
 &= O_{ff}|_{300K} - (1 - O_{ff}|_{300K}) \frac{\partial E_{gb}(T) - \partial E_{gw}(T)}{E_{gb}|_{300K} - E_{gw}|_{300K}}
 \end{aligned} \tag{2.1}$$

The simulation considers the temperature dependence of the carrier mobilities $\mu_{n|p}(T)$, in fact the capability of the carriers to overcome the EBL potential barrier and to escape the QWs are both phenomena affected by the carrier mobilities.

Two different values of the exponential factor are considered for the electron and hole mobility: $\alpha_n = 1.5$, $\alpha_p = 2$ [19].

The SRH lifetime $\tau_{n|p}(T)$ for electrons and holes is evaluated with the low temperature approximation with $\beta_{n|p} = 1.5$ [20], correct in the range of temperatures simulated. This trend is the typical choice, however for instance a linear behaviour is extrapolated by *Zhao et al.* [23].

The spontaneous recombination rate $B(T)$ is kept constant at the value reported in table B.2. Regardless, a trend in temperature is evinced with some discrepancies in the literature. Given the equation in table 2.1, different values of γ can be applied. *Tian et al.* [24] suggest a different dependence as the carrier injection changes: $\gamma = 4$ with $n = 2 \times 10^{18} \text{ cm}^{-3}$, $\gamma = 1.5$ with $n = 1 \times 10^{20} \text{ cm}^{-3}$. *Zhao et al.* [23] have extrapolated $\gamma = 1.5$ without considering the dependence on injection, while *De Santi et al.* [19] apply $\gamma = 2$.

The Auger coefficient $C(T)$ is another parameter that could be found with different thermal trend depending on the literature in which we are relying. For *Tian et al.* [24] the Auger coefficient empirically follows $C(T) \propto T^{-2}$ with $n = 1 \times 10^{20} \text{ cm}^{-3}$ and with temperatures greater than 300 K. This proportionality is contrary to most theoretical and experimental trends, like for example *Bertazzi et al.* [27]. However the range of temperature considered by these references are near 300 K or above and therefore, the two behaviours reported are not of our interest. Besides, the trend reported in table 2.1 is applied to the simulations and it is valid for the range 100-350 K [25].

For what concerns the activation energies of the impurities in the doped layers of the devices, a thermal dependence of the acceptor energy in the GaN should be considered. But since the constant value starts to decrease for temperatures above 350 K [26], the activation energies of 170 meV and 200 meV for the p-doped GaN and the EBL, respectively, were kept constant [9]. We must also remember that the ionization energy depends on the concentration of the dopants which increasing causes the decrease of the activation energy [28] and therefore, the diffusion of impurity atoms due to an high working temperature could affect their ionization capability.

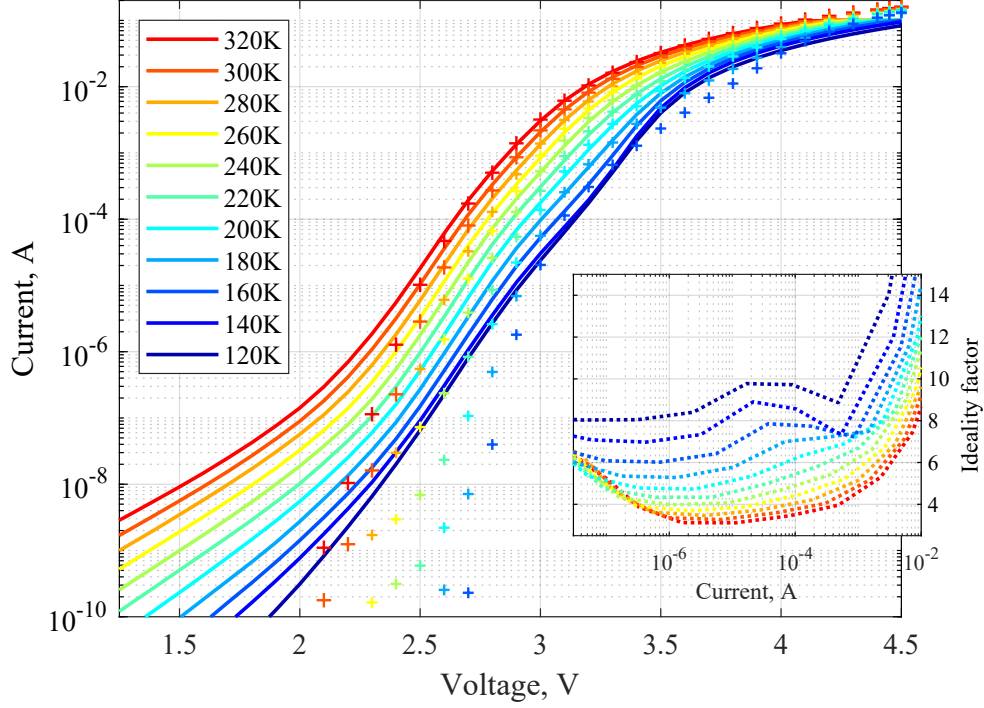


Figure 2.1: Temperature dependent IV characteristics, experimental measurements in solid lines, simulated results as scattered plot (logarithmic scale). Experimental temperature dependent ideality factor in the side plot (current axis in logarithmic scale).

2.3 IV characteristics

As announced in the previous section, the contact resistance $R_c(T)$ and the fraction of polarization charges $x_{pol}(T)$ are varied in order to agree with the IV characteristics (see Fig. 2.2) [29]. The series resistance affects the slope of the IV curve in the region above 3.5 V, making possible the current saturation. Besides, the effect of the polarization charges is relevant between 2.5 V and 3.5 V. For lower biases the agreement is not achievable, in fact the simulated IVs have a higher slope and a lower value of current. The disagreement appears in the region where the voltage is too low to have the carrier transport towards the abrupt potential steps present in the junction (see the band diagram). The experimentally observed current for low biases must be associated with the tunneling phenomenon. *Mandurrino et al.* [30] had verified that the application of the trap-assisted tunneling (TAT) gives the possibility to increase the current flow with a small external po-

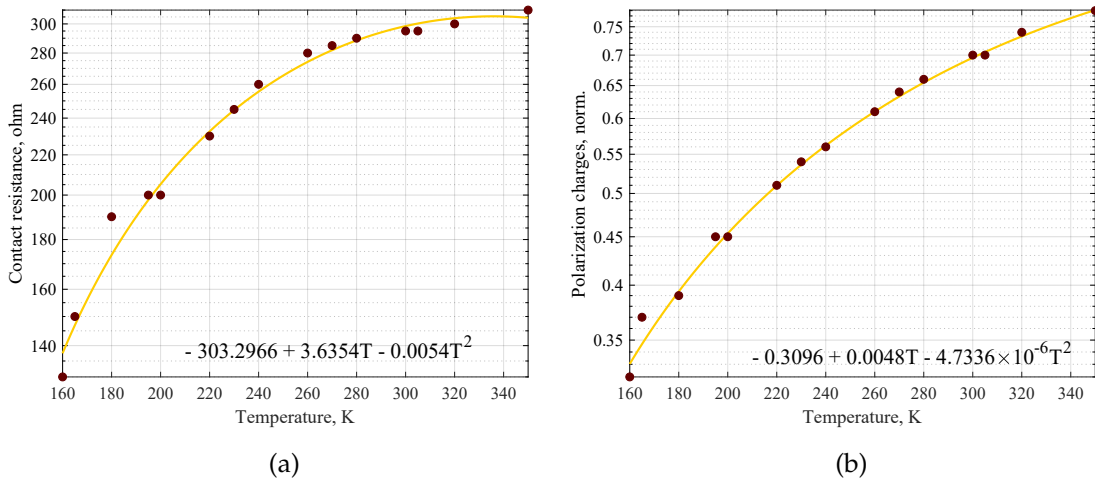


Figure 2.2: (a) Extrapolated temperature trend of the contact resistance $R_c(T)$ with fitting curve. (a) Extrapolated temperature trend of the fraction of polarization charges $x_{pol}(T)$ with fitting curve.

larization, nonetheless their simulation without the tunneling effect has a trend comparable with ours. Furthermore, the simulated IV starts to lose the correct behaviour for the whole range of voltages when the temperature is below 160 K.

2.4 Investigation on the thermal droop

Several factors play a fundamental role when predicting the thermal trend of the efficiency. In order to give a clear idea, we will proceed by listing those factors and by giving a summarizing description of their effect.

The injection efficiency defines the part of carriers that actually reaches the quantum wells in the active region and does not escape crossing the EBL layer. Its magnitude is related to the carrier mobilities, which lead to a considerable dependence in temperature. In fact, the fraction of carriers leaving the well increases with their mobility. In other words, when the carriers enter the well, they are typically placed in the fundamental confined states. From this energy level they can recombine themselves or escape. In this situation, the energy of the carriers is given by the thermionic emission model in which the temperature has a key role. This phenomenon generates the so-called **leakage current**.

The SRH recombination comes into action when the carriers reach the inside of the well. Its role is to keep in consideration the presence of a defect density in-

side the active region of the LED that leads to a non-radiative recombination process. The impact of the SRH recombination is important for low current densities and it depends on the trap density, the carrier velocity and the capture cross section of the defects [11]. While the middle range of current density is dominated by the radiative processes, the second contribute to the carrier recombination. Nonetheless, the energy level of the trap, situated inside the energy gap, defines the magnitude of the recombination. As a matter of fact, if we are in presence of trap levels in proximity of the energy gap mid-point the SRH recombination process is enhanced. As a final remark, the defect density can be distributed in a certain way depending on the doping and the composition of InGaN layers. In the latter case a value of about 0.24 of the In molar fraction can easily improve the dislocation density and the composition fluctuations [2]. The In molar fraction fluctuations can reduce the volume of the light-emitting active region because of carrier localization in proximity of the sections with highest In molar fraction.

The Auger recombination is the final contribute to the recombination in the active region. Differently from the SRH and from the radiative processes, a third carrier acquires the energy related to the e-h pair recombination in order to achieve a final state with an energy higher than before. In addition, its magnitude is significant for high carrier densities.

2.5 EL intensities

We will now deepen our understanding of the LED thermal behaviour comparing the experimental EL spectra with simulations, where the temperature dependences follow the description given in section 2.2. The experimental EL intensities at 5 mA and 100 mA (see Fig. 2.3.a, 2.3.b) show both a secondary peak for temperatures below 230 K, with increasing maxima as the temperature decreases (see Fig. 2.3.c and 2.3.d). *Wang et al.* [31] had found a comparable experimental behaviour for temperatures below 200 K, also they were studying a structure similar to ours. In their work the presence of this secondary peak (see Fig. 2.5.a) is related to the temperature dependence of the defect density in the well near the n-side, which in our case is the blue QW. So, the capture rate of the blue QW would be enhanced at low temperatures increasing the radiative recombination

of the carriers because the defect density would be frozen. However, in our case the magnitude of the secondary peak with respect to the primary one is not important as in their work and this explanation would be in contrast with the hole concentration profile at low temperature. In fact, the small hole mobility makes it improbable to have an uniform concentration in the blue QW too, reason why the secondary peak should not be associated to this well. We also have to consider that at low temperature the hole concentration is globally lower because of a small ionization of the p-GaN dopants, creating the effect called freeze-out. In addition, the wavelength of the secondary peak is about 390nm while the blue QW emits for a value of about 420nm, as verified in the Fig. 1.4 for structure A and B.

A more appropriated explanation is given by *Shin et al.* [32] in which a side peak is seen to grow at about 400 nm as the temperature is lowered from 300 K. The side peak is thought to originate from the Mg acceptor level in the p-GaN and is caused by the electrons overflowing to the p-GaN cladding layer. The researchers think that the growing overflow with decreasing temperature basically originates from the saturation of the radiative recombination rate at a smaller current and from the decrease of the nonradiative recombination rate. In other words, the degree of saturation in the radiative recombination rate increases as the effective active volume; which becomes smaller than the nominal one for two reasons: first, the QWs in the active region are not fully utilized due to the carrier transport problem caused especially by holes in the conventional LED structure and second, even in a fully utilized QW, the effective volume would be smaller than the nominal QW volume since In in the QW tends to cluster, making the region with less indium content inefficient in emitting light. Also, with higher indium concentration in the QW, the piezoelectric field becomes higher, impacting in a negative way the radiative recombination rate.

Another minor feature of the experimental spectrum in Fig. 2.3.a is the appearing of a small projection on the left side of the secondary peak just for high carrier injection. A possible explanation could be the radiative recombination on the left side of the EBL. This supposition is based on the relation of the energy gap and the emission wavelength; in fact, the wavelength related to this projection can only be associated to a GaN barrier in the structure C. This feature

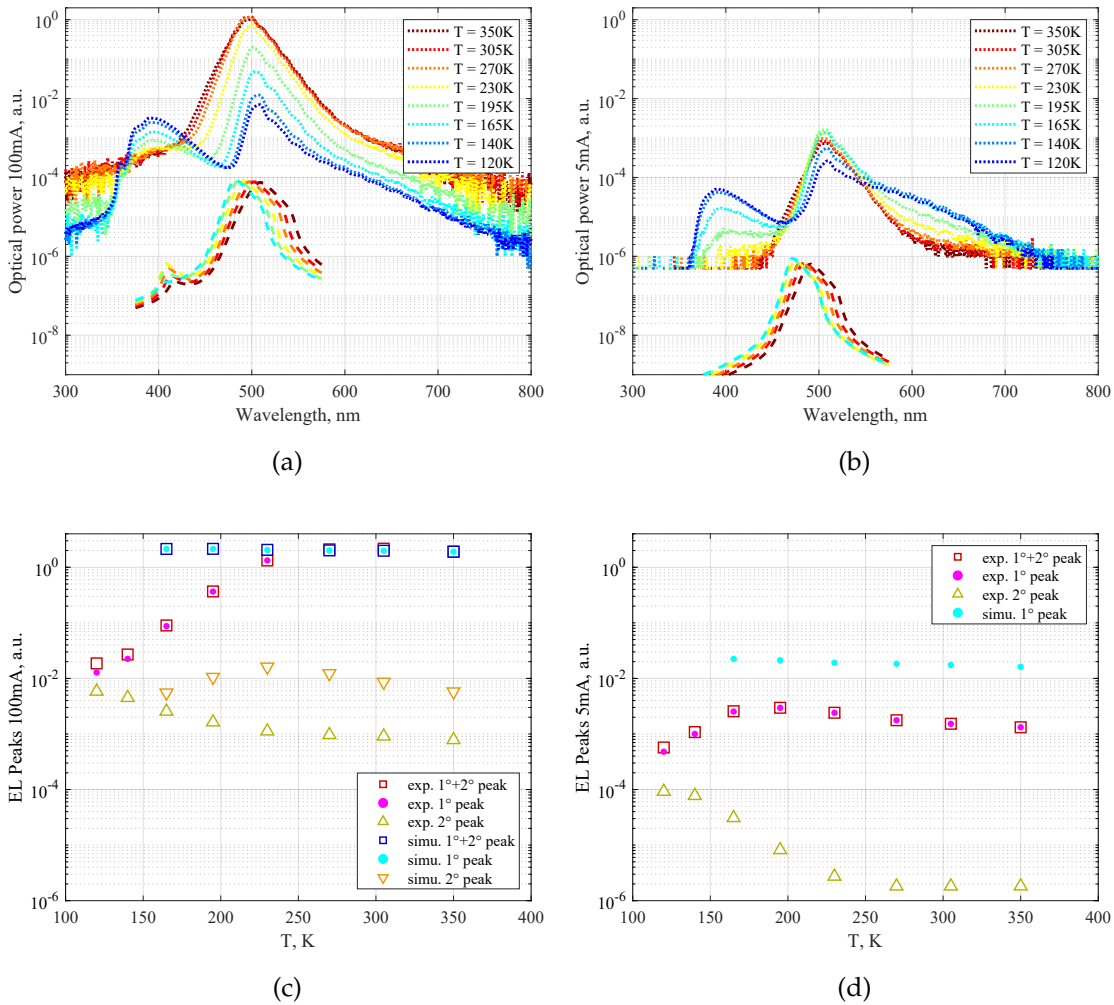


Figure 2.3: (a) Experimental (dotted lines) and simulated (dashed lines) EL intensities as a function of the temperature at 100 mA, both reported in arbitrary unit and not comparable in terms of absolute value. (b) EL intensities at 5 mA. Fig. (a) and (b) are comparable. (c) Trend with respect to the temperature of the peaks at 100 mA. Simulated and experimental peaks are normalized to have agreement of the sum of the two peaks at 350 K. (d) Trend of the peaks at 5 mA. Fig. (c) and (d) are comparable, indeed the normalization used in (c) is kept.

appears only at high current injection, because a high np product is necessary to achieve radiative-recombination in the gallium nitride barrier.

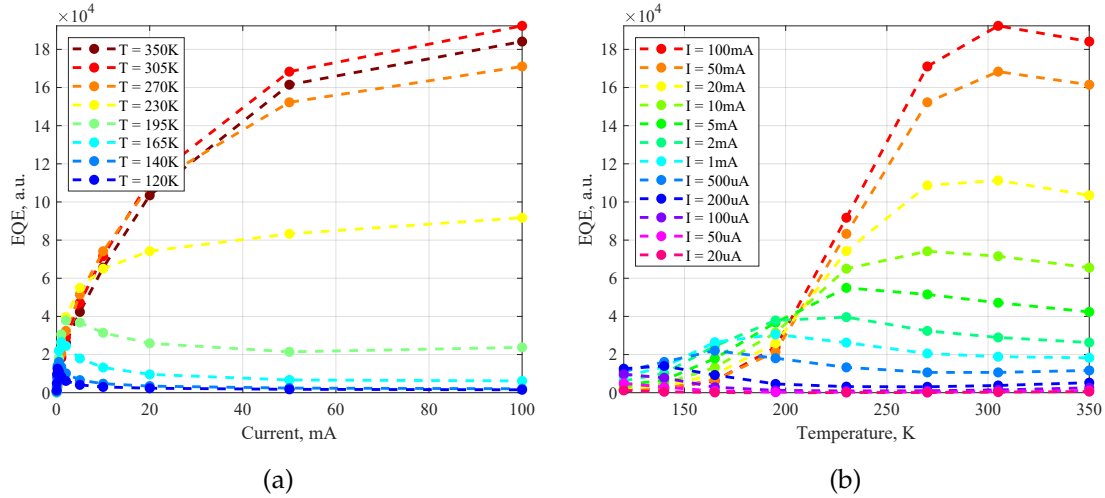


Figure 2.4: (a) Evaluated experimental EQE with respect to the current flow for the range of temperature of the measured EL spectra. (b) Evaluated experimental EQE with respect to the temperature for the range of current values of the measured EL spectra.

For what concerns the trend of the primary peak (see Fig. 2.3.c, 2.3.d), it follows the globally recognized monotonal decrease [33]–[43] as the temperature increases only for low carrier injection. In fact, the experimental spectrum in Fig. 2.3.b is reported as the threshold of this behaviour, meaning that there would be a certain current for which the primary peak has an almost constant value as the temperature changes. The trend is opposite for currents above 5 mA; while the maximum of the peak increases with the temperature, it remains constant between 270–305 K and starts to decrease as soon as it goes beyond those values, a more detailed view is given by the EQE as a function of the temperature (see Fig. 2.4). Given our unpredicted experimental results, an important research in the literature has been performed in order to find particular cases similar to our and to collect the opinions of the researchers.

We can start by naming *Han et al.* [44] who suggest that the efficiency increases with the temperature because at low temperatures the total recombination rate in the active region becomes saturated for low current densities, as mentioned before when describing the presence of the secondary peak. Their EL spectra are reported in Fig. 2.5.d. The same explanation is given by *Shin et al.* [32], where

the IQE as a function of the temperature switches its behaviour at 1 mA (see Fig. 2.5.c).

In *Dalapati et al.* [45], when temperature is lowered below 228 K, the light intensity instead of increasing starts decreasing for currents above 10 mA (see Fig. 2.6.a). In their study, the limiting injection current (LIC), that indicates the transition point from non-radiative to radiative recombination, is supposed to be the main issue from which we should start to think of a deeper explanation. Actually, the LIC shifts to lower injection regime with the lowering of the temperature (see Fig. 2.6.b, note that only the curve related to LED1 has to be considered in relation to Fig. 2.6.a).

In *Prudaev et al.* [46] [47] the ballistic transport of charge carriers is taken into account. In this work, the authors remind to the readers that the mean free path of electrons must be increased when the temperature decreases. Furthermore, with decreasing temperature, ballistic leakage can be increased due to the increase of the potential energy of the electrons injected into the active region. Since the resistance of MQW is increased with a decrease in temperature, the voltage drop at the same current densities will also increase with decreasing T and, as a result, the potential energy of electrons must be increased due to the voltage applied to the MQW region. Nonetheless, from their simulated EQE (see Fig. 2.6.d) a decrease in the MQW thickness, that is a decrease in the resistance, shifts the dependence of EQE to lower currents, which explains qualitatively the experimentally observed temperature inversion of the EQE (see Fig. 2.6.c). According to this model, the effect of temperature inversion of the EQE should be minimized in samples with small thicknesses of the active region. An experimental evidence has been found by *Wang et al.* [48], where different measures of the EQE had been performed with different QW thickness (see Fig. 2.7.a).

As a final consideration, a possible misunderstanding in the temperature characterization is reported in Fig. 2.7.b, 2.7.c. Where the EL intensities increase as the temperature increases, while the evaluated EQE decreases. This example is somehow the proof of the controversial temperature dependence of the GaN-based LED and of the reason why the problem should be treated carefully.

For what concerns the simulations, the trend of the primary peak is decreasing monotonally as the temperature increases independently of the amount of

current density (see Fig. 2.3.a and 2.3.b). The red-shift of the spectra as the temperature increases is related to the temperature dependence of the energy gap of the QWs. Actually, the energy gap is defined by the Varshni model (see equation A.5), where the energy gap is inversely proportional to the temperature, leading to higher emission wavelength of the active region as the temperature increases. The reduction of the energy gap with the temperature is also a consequence of the efficiency decrease for high temperature. As a matter of fact, the injection efficiency of each QW is lowered as the energy gap decreases because a smaller fraction of carriers is able to reach the inside of the well. Moreover, the overall red-shift as the current injection increases is related to the application of the many-body interactions with the parameter called exchange coefficient (see equation 1.12), where the shift towards higher wavelengths is proportional to the carrier concentrations in the QWs.

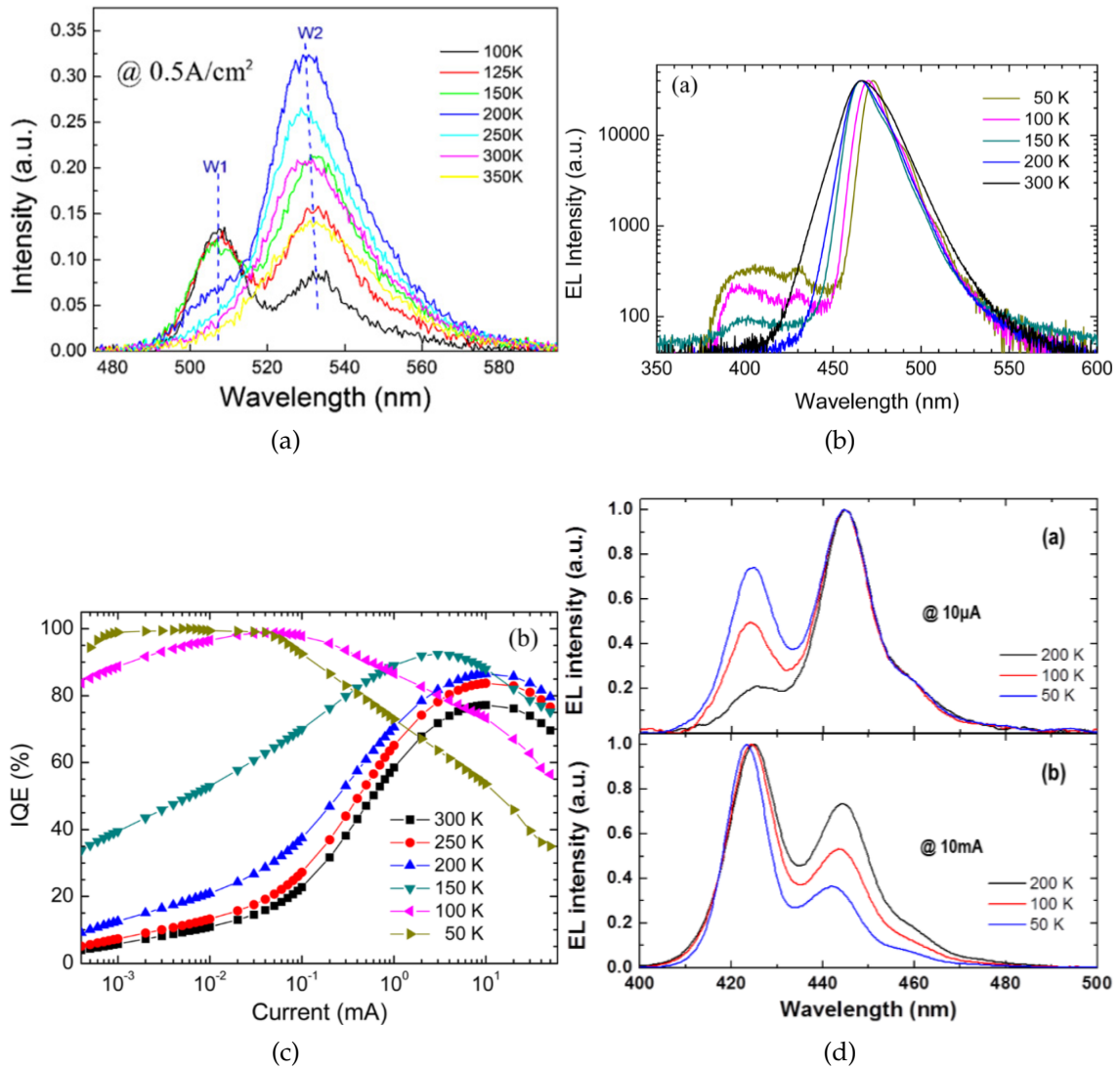


Figure 2.5: (a) Fig. from Wang *et al.* [31]. (b) Fig. from Shin *et al.* [32]. (c) Fig. from Shin *et al.* [32]. (d) Fig. from Han *et al.* [44].

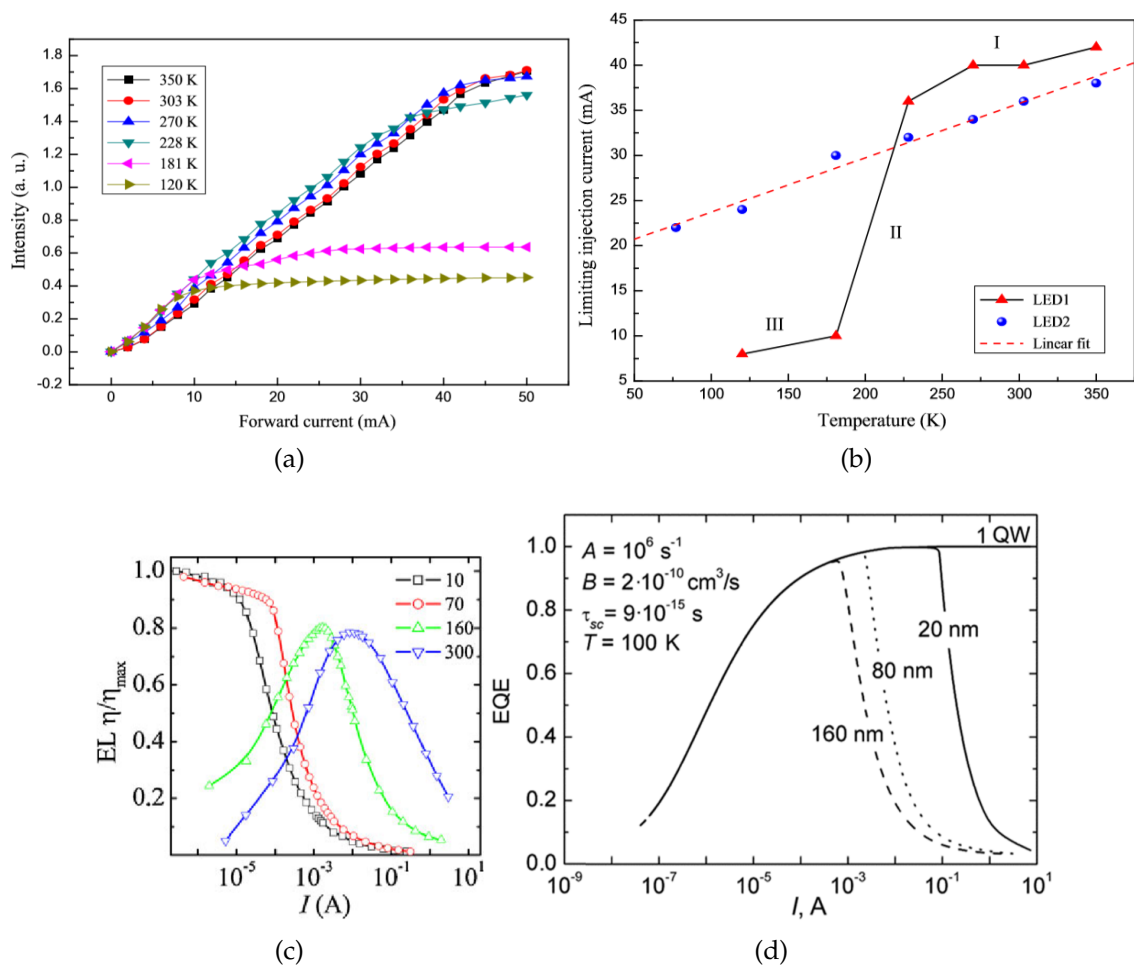


Figure 2.6: (a) Fig. from Dalapati et al. [45]. (b) Fig. from Dalapati et al. [45]. (c) Fig. from Prudaev et al. [46]. (d) Fig. from Prudaev et al. [47].

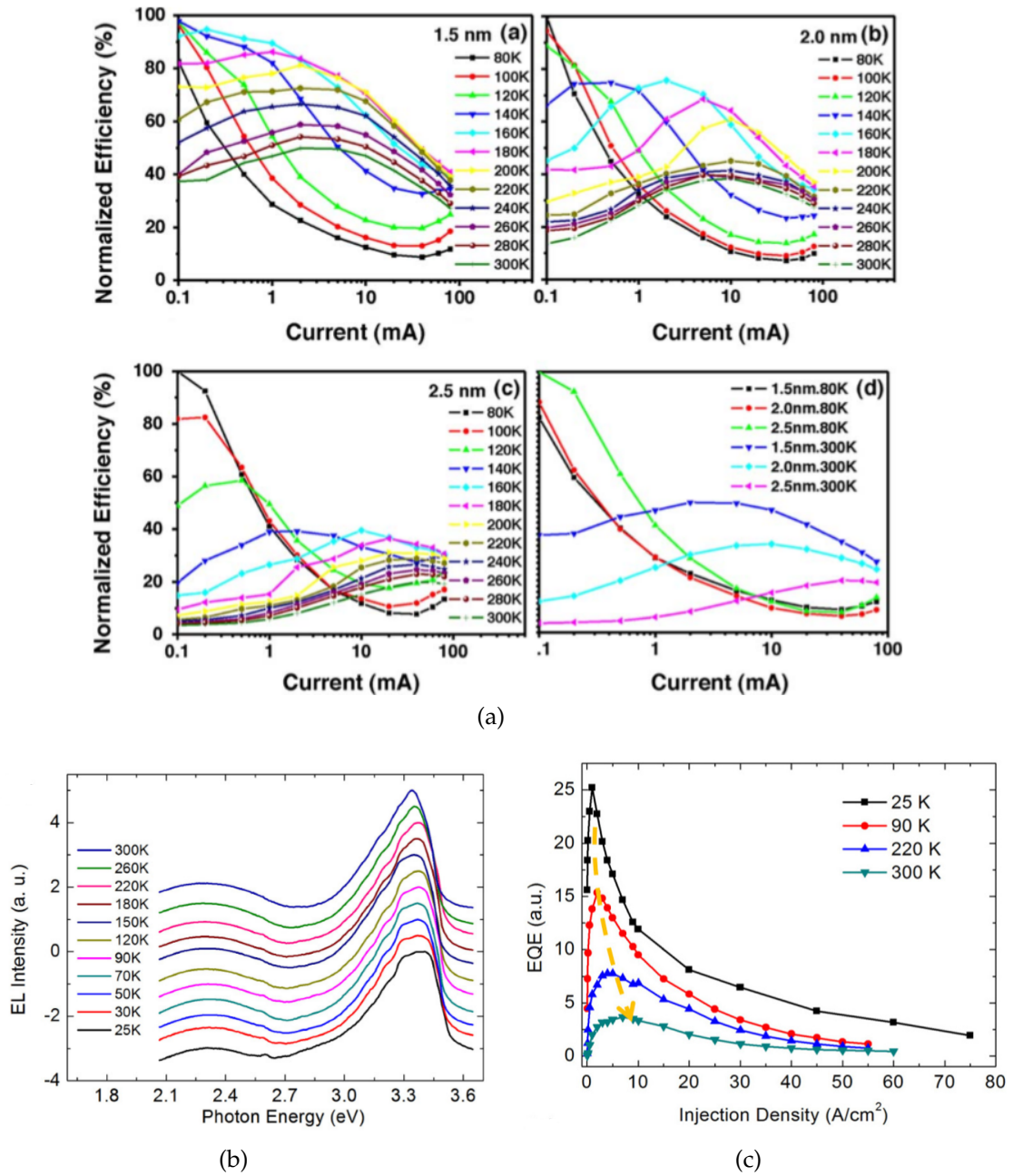


Figure 2.7: (a) Fig. from Wang *et al.* [48]. (b) Fig. from Wang *et al.* [49]. (c) Fig. from Wang *et al.* [49].

InGaN/GaN MQW solar cells

3.1 Introduction

The following chapter is divided in three parts: we will start by introducing the main parameters used to characterize a solar cell, as the open circuit voltage, the short circuit current, the fill factor and the conversion efficiency. We will then proceed describing the structures of the analyzed InGaN/GaN MQW solar cells and presenting the simulations; we will notice many similarities with the simulations performed on the GaN-based LEDs. In the final section we will depict a comparison between the experimental evidences and the results of the simulations.

3.2 Electrical characterization of a solar cell

Most of the information that we can obtain about the performance of a solar cell is contained in the JV characteristic. The generation of carriers in the cell induces, thanks to the separating built-in potential, a photo-generated current which flows through a load. It can be considered as a simple resistor, which, by generating a voltage, polarizes the solar cell. As a result, the working condition of the cell depends on both the photo-generated current and the load.

We start by considering an equivalent circuital model where the dark current is represented by a diode having an ideal characteristic. The photogenerated current I_P is considered constant and generated by solar radiation (see equation 3.1) and it makes the JV characteristic shift in the third and fourth quadrant, the latter

being called photovoltaic region.

$$I = I_S(e^{V/V_T} - 1) - I_P \quad (3.1)$$

The evaluation of the device performance is then carried out by evaluating two main parameters: the open circuit voltage and the short circuit current, where the open circuit voltage is produced by the cell under illumination in open circuit configuration and is analytically evaluated by imposing the total current equal to zero. Here follows the voltage measured at the edges of the device:

$$V_{OC} = V_T \ln \left(\frac{I_P}{I_S} + 1 \right) \quad (3.2)$$

The short circuit current is calculated as the current flowing with no voltage applied at the contacts of the device. The resulting value is simply the photo-generated current:

$$I_{SC} = -I_P \quad (3.3)$$

The V_{OC} and the I_{SC} can be related by simply defining the overall behaviour of a solar cell. The self-generated potential V_{OC} can be explained by the generation of carriers in the semiconductor that, through Poisson's equation, results in a potential over the junction. This generated potential forces the cell out of equilibrium with a direct polarization to compensate the motion of carriers. Now, if we hypothesize that we are passing from the open circuit configuration to a configuration with a load applied to the contacts of the solar cell, part of the bias is lost because of the current flowing through the contacts. The balance is achieved with a final shift of the characteristic in terms of voltage and current. At the end, we will have the classical fourth quadrant of the JV of a solar cell, where the negative current decreases and the positive voltage increases as the optical power of the illumination increases.

In order to exploit the whole potential of the cell, the voltage on the cell itself has to be tuned so to reach the optimum power density in the JV characteristic. Indeed, the maximum of the power obtainable from the solar cell can be therefore

extrapolated by applying a bias on the junction (see equation 3.4).

$$P_m = I_m V_m \quad (3.4)$$

These values can be used for the computation of the fill factor (FF):

$$FF = \frac{I_m V_m}{I_{SC} V_{OC}} \quad (3.5)$$

The FF can also be seen as the ratio between the area of the JV fourth quadrant and the area produced by the product of the maximum operating current density and voltage. Indeed, the FF cannot be higher than 1. We should also consider that, a $FF=1$ cannot be obtained since it would require no voltage drop even in series resistances and a perfect conversion of the incoming light in electrical current. Carrier recombination due to surface effect, standard bulk scattering events, imperfections in the electrical contacts, are all factors which contribute to lowering the fill factor and thus the efficiency of a real cell.

Finally, the important figure of merit of the system is the power provided by the solar cell which, of course, is strictly smaller than the product $P_{max} = V_{OC} I_{SC}$, meaning that these two quantities can be taken as limiting values for the system. Finally, the maximum power found is used to evaluate the power conversion efficiency, which is the upper bound of the efficiency obtainable by a solar cell:

$$\eta = \frac{I_m V_m}{P_{inc}} \quad (3.6)$$

3.3 Mesa structures: QW thickness, EBL and HBL

The studied solar cells have an n-GaN/i-MQW/p-GaN design grown on c-plane sapphire. The active region is decomposed in a certain number of InGaN/GaN QWs, colored in light green in Fig. 3.1. All the QWs feature a 15% In molar fraction, and are sandwiched between a thick n-type GaN layer and a p-type GaN layer. The main differences between the structures are the number of QWs in the active region, the presence of p-type AlGaN EBL ([Mg] $N_A = 2 \times 10^{19} \text{ cm}^{-3}$) and of n-type AlGaN HBL ([Si] doping value not given) with varying thicknesses and constant Al molar fraction with value 0.15. The thickness of the top p-type

Table 3.1: Structure designs of the GaN-based solar cells.

Sample	p-GaN [nm][cm ⁻³]	EBL [nm]	MQW [nm]	HBL [nm]	n-GaN [nm][cm ⁻³]
C	100	0	25 QWs	0	2000
	5×10^{17}		InGaN(2.2) GaN(4.8)		5×10^{18}
Ref	100	0	30 QWs	0	2000
	2×10^{19}		InGaN(3) GaN(7)		3×10^{18}
1A	100	5	30 QWs	0	2000
	2×10^{19}		InGaN(3) GaN(7)		3×10^{18}
1B	100	10	30 QWs	0	2000
	2×10^{19}		InGaN(3) GaN(7)		3×10^{18}
1C	100	5	30 QWs	5	2000
	2×10^{19}		InGaN(3) GaN(7)		3×10^{18}
2A	50	5	30 QWs	0	2000
	2×10^{19}		InGaN(3) GaN(7)		3×10^{18}
2B	150	5	30 QWs	0	2000
	2×10^{19}		InGaN(3) GaN(7)		3×10^{18}

GaN layer is changed in order to verify the variation of absorbed light outside the active region (see table 3.1 for all the values, the sample names are consistent with the references). In Fig. 3.1 the structure of sample 1C is presented. The solar cell 1C is in fact the only analyzed structure with the HBL, which makes it the most complex. All structural data depicted above are taken from *Dogmus et al.* [2] and *Huang et al.* [50].

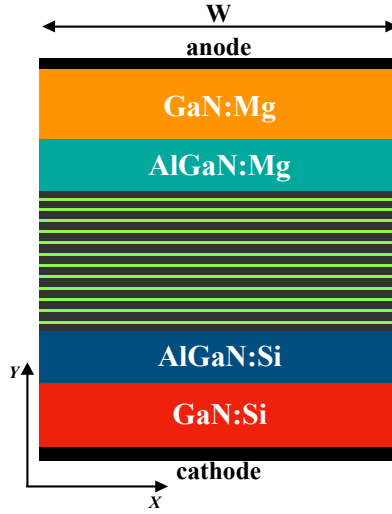
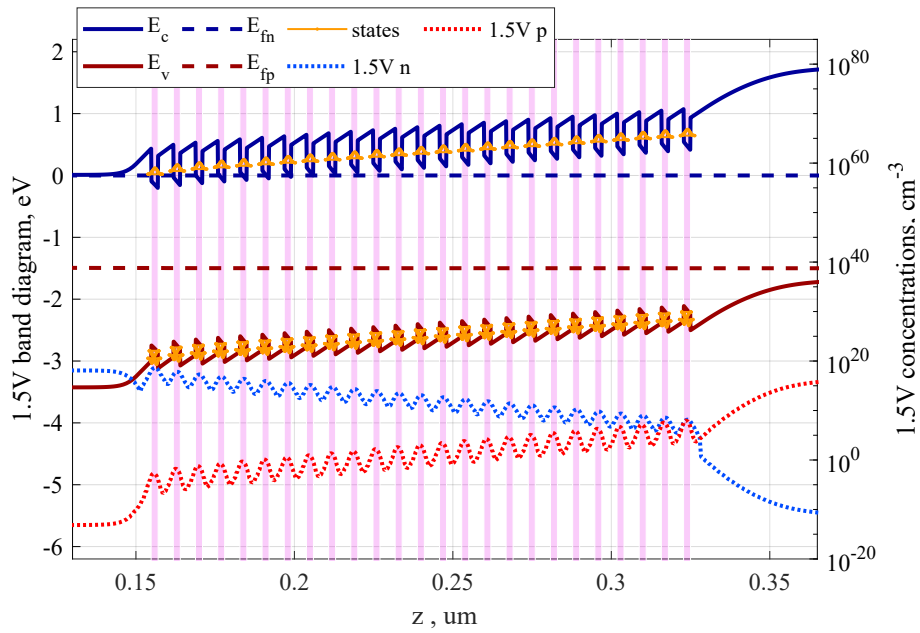


Figure 3.1: Simulated 1D geometry of structure 1C. The apparent width of the column-shaped device along the \vec{x} direction is fixed to $500\mu\text{m}$, however the results will be reported as quadratic densities. The figure is not drawn to scale.

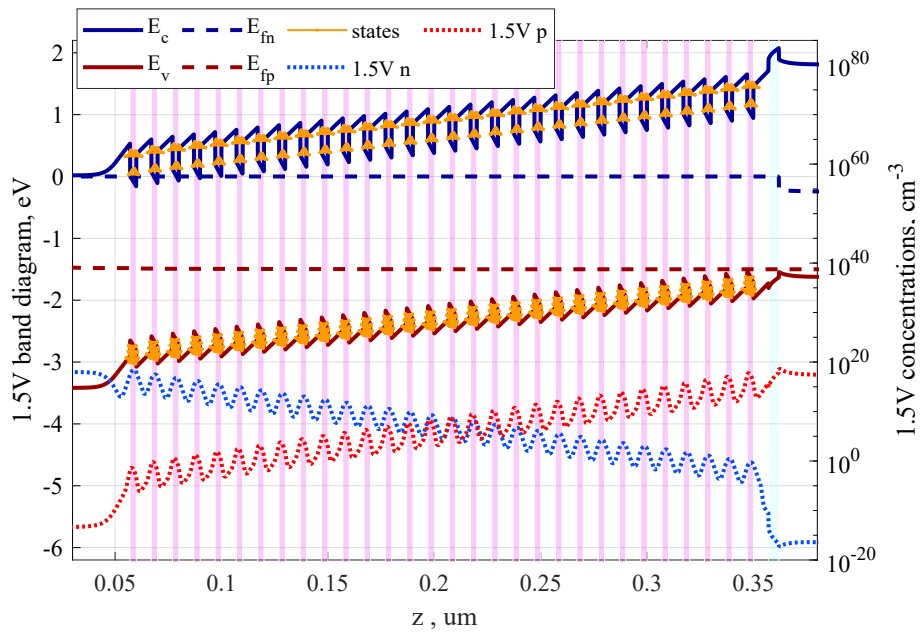
3.4 Analysis of the results

Before simulating the entire structures, a preliminary study of devices including a smaller number of QWs has been performed in order to verify the quality of the simulations and to execute some parametric studies. The used set of parameters is summarized in the tables 1.2 and B.2; the only difference is the value of the wave-range, which depends on the QW and barrier thickness: $\Delta_{wave} = 3\text{ nm}$ for structure C and $\Delta_{wave} = 4\text{ nm}$ for all the other structures.

We will start commenting the variety of designs presented in table 3.1. The presence of the EBL and the HBL is one of the aspect that differs in the geometries. From the experimental results obtained by *Huang et al.* [50], we can see that the efficiencies of the structures having at least one blocking layer is dramatically increased, almost doubled (see table 3.2). This unconventional result seems to contradict the reason why the blocking layers are used in opto-electronics. As a matter of fact, the blocking layer is placed next to the last QW barrier in order to achieve a higher carrier concentration in the active region and to reduce the leakages, but in any solar cell the main purpose is the extraction of the generated carriers from the active region. The EBL in structure 2A does not affect the electron concentration, as it can be seen from Fig. 3.2.b where the bias is fixed at 1.5 V



(a)



(b)

Figure 3.2: [T=298 K] (a) Band diagram of structure C at 1.5 V with confined states of the QWs and carrier concentrations. (b) Band diagram of structure 2A at 1.5 V, figure depicted as the one at equilibrium. The QWs and the EBL are highlighted with light colors.

to stay near the working region of the solar cell.

A possible answer to this reaction could be the fact that the structures with the blocking layers have a higher quality of growth with respect to the structures which do not. This final remark is consistent with the shapes of the EL intensities. In fact, if we look at Fig. 3.3 the agreement between the simulations and the measurements is much more significant for structure 2A with respect to structure C. Also, it must be remembered that the QWs of structure C are thinner, meaning that their composition quality is probably worse.

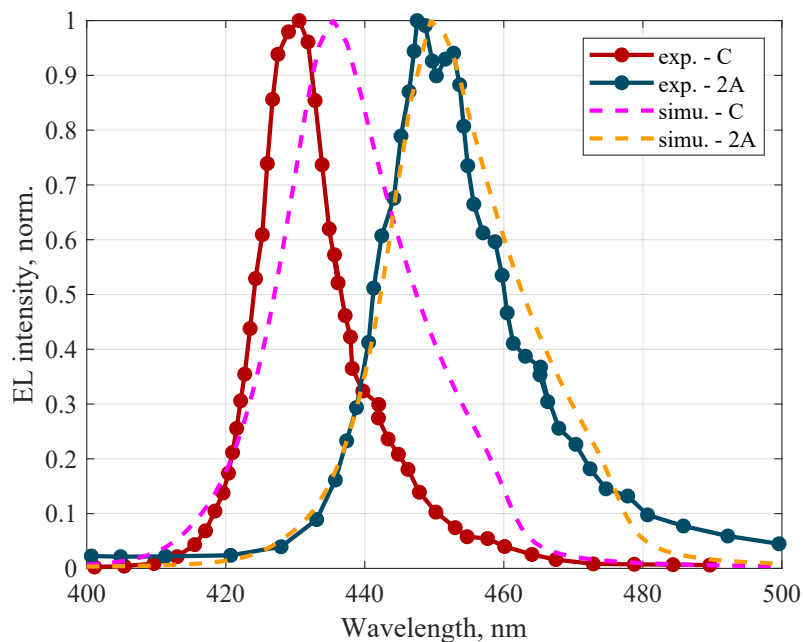


Figure 3.3: [T=298 K] Experimental and simulated EL intensities of the structures C and 2A. All data are normalized to the maximum peak.

However, the operation of a solar cell differs from that of a LED. In fact, the working point of a solar cell presupposes a reverse current in the junction (the sum of the dark and generated current) and, therefore, the electrons flow towards the n-side (on the left in our band diagrams) and the holes towards the p-side. In this way the blocking layers should help to separate the two carrier families and to avoid a high rate of recombination outside the active region. These final consequences are not necessarily true, since the EBL generates a small potential barrier also in the valence band depending on the value of the band offset. This means that the hole flow is affected by the EBL and the electron flow by the HBL.

As it can be easily understood, the presence of the blocking layers can radically affect the behaviour of these structures and give much uncertainty to the simulations. For these reasons the study continues with the characterization under the AM1.5g solar spectrum.

3.4.1 Performances under AM1.5g solar irradiance

Before giving a closer look to the results, it seems necessary to report a brief introduction about the connection between the GaN-based solar cells and their application under the solar irradiance. The solar spectrum has a specific shape resolved in wavelength, in which a flat region of maximum intensity is situated in the wavelength range 430-680 nm (see Fig. 3.4.b). In view of exploiting this wavelength range, InGaN/GaN MQW solar cells allow to cover the left extreme (the starting point of the UV area) of the wavelength range with maximum intensity; in Fig. 3.4.b the yellow band represents the working region of our devices, where

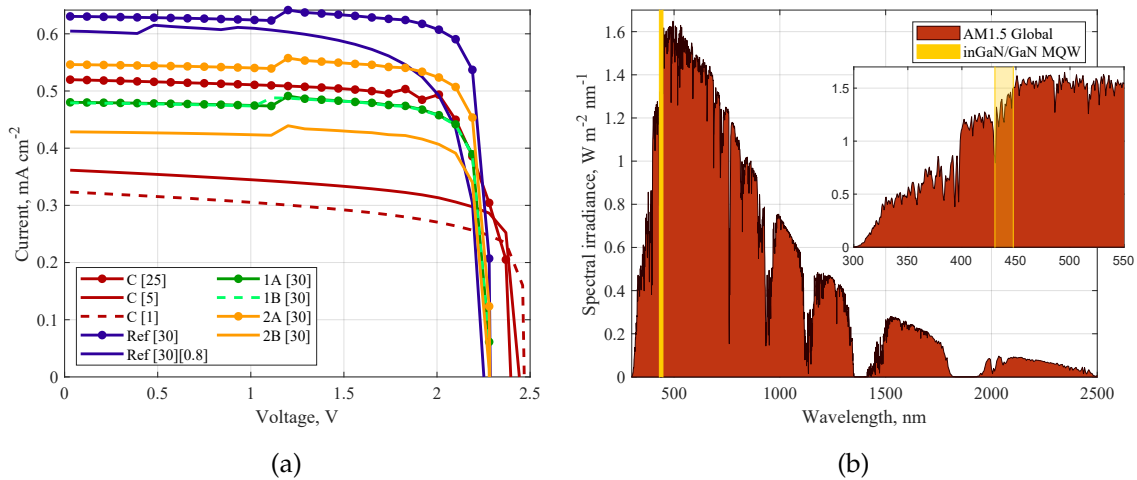


Figure 3.4: [T=298 K] (a) JV characteristics under AM1.5g illumination. (b) AM1.5g solar spectrum; the two extremes of the yellow region are the wavelengths related to maximum peaks of EL intensity of structure C and 2A (zoom in the significant region in the side plot).

the left side of the yellow band is given by the wavelength of the maximum EL intensity of structure C, while the right side is evaluated with the same concept but for the structure 2A. As a consequence of this limited absorption range the conversion efficiencies are considerably small compared to the values in the global

market. However, the InGaN/GaN MQW solar cells are designed to work in a more complex structure as the multi-junction concept, meaning that the values of efficiency found experimentally and with the simulations are only for research purposes.

In table 3.2 are reported the main parameters related to the performances of the solar cells: open circuit voltage, short circuit current density, fill factor and conversion efficiency; the simulated JV characteristics, from which the parameters have been extracted, are reported in Fig. 3.4.a, while the experimental JV characteristics can be found in the two references [2], [50].

In the case of structure C the parameters are given for a variable number of QWs in the active region, here we can see the importance of simulating the whole structure in order to reach a reasonable J_{SC} . However, the simulated J_{SC} are generally low with respect to the experimental ones.

Another parametric study has been carried out changing x_{pol} in the structure Ref. However the only appreciable effect here is a decrease of the FF as the polarization charges increases.

Generally, the experimental FF is smaller, as it can be noted from the curvature of the JV characteristics in the references [2], [50]. This must be related to the presence of defects and composition fluctuations inside the active regions, leading to a small shunt resistance that degrades the V_{OC} and the FF . In particular, the experimental V_{OC} of structure C is drastically lowered by the density of defects inside the active region, which must be connected to the smaller thickness of the QWs.

For what concerns the J_{SC} , from the structures without the blocking layers (C and Ref) we can understand that the thickness of the QWs affects the performances of the solar cells. Actually, the J_{SC} decreases as the QWs get thinner both in the experimental measurements and in the simulations. In fact, as we can see from the band diagrams in Fig. 3.2, the number of available confined states is bigger as the thickness of the QWs increases, meaning that we have absorption for more wavelengths and more states for the generation of carriers.

Going back to the problem related to the EBL (Ref: none, 1A: 5 nm, 1B: 10 nm), we see how the experimental J_{SC} increases as the EBL thickness increases while for the simulations the trend is strictly contrary.

Table 3.2: Device performances of the InGaN/GaN MQW solar cells ([e/s] [QWs] [x_{pol}] = [experimental/simulated] [number of QWs] [fraction of polarization charges]). $x_{pol} = 0.4$ when not reported.

Sample	[e/s][QWs] [x_{pol}]	V_{OC} [V]	J_{SC} [mAcm ⁻²]	FF [%]	η [%]
C	[e][25]	1.66	0.65	49.60	0.52
C	[s][25]	2.39	0.52	79.66	0.99
C	[s][5]	2.44	0.36	73.95	0.65
C	[s][1]	2.47	0.32	70.73	0.56
Ref	[e][30]	2.09	0.87	52.57	0.95
Ref	[s][30]	2.29	0.63	86.04	1.24
Ref	[s][30][0.8]	2.25	0.60	73.99	1.01
1A	[e][30]	2.18	1.36	59.27	1.77
1A	[s][30]	2.28	0.48	84.63	0.93
1B	[e][30]	2.17	1.43	54.31	1.69
1B	[s][30]	2.28	0.48	84.57	0.93
1C	[e][30]	2.15	1.31	59.70	1.66
2A	[e][30]	1.66	1.49	63.17	1.57
2A	[s][30]	2.28	0.55	85.34	1.06
2B	[e][30]	2.15	1.27	59.04	1.62
2B	[e][30]	2.28	0.43	84.06	0.82

Finally, the increase of the p-GaN thickness (2A: 50 nm, 2B: 150 nm) has the effect of decreasing the J_{SC} in both the experimental measurements and in the simulations. This is a reasonable behaviour since the thickness of the p-side must be minimized in order to avoid light absorption outside the active region. Actually the e-h pairs generated outside the active region have a higher probability to recombine, because the built-in electric field is not strong enough to divide the pair.

Conclusions

This research aimed to identify effective strategies to match the quantum-corrected drift-diffusion electro-optical models with the experimental characterizations through a campaign of iterative parametric studies. The results indicate that potential improvements in the understanding of GaN-based LEDs and solar cells can be achieved following this iterative methodology. Moreover, the yield of the final outcomes has been improved by the slight differences between the geometries of the devices, that made it simpler to determine a finer selection of the simulation parameters. As a matter of fact, we have highlighted the main physical aspects required to work with devices based on nitride alloys:

- The importance of the interface charges caused by the spontaneous and piezoelectric polarization, which lead to a reduction of the current flow in the structures of several orders of magnitude and consequently to a decrease in terms of efficiency; for this reasons they are proposed for the IV and EQE matching. An experimental measurement in temperature of the profile of the interface charges would be a significant step forward to establish a fixed value of the fraction of polarization x_{pol} .
- The application of a series resistance is the key to achieve an important agreement at high current injection in the LEDs. We can take into consideration that the interface between the contact pads and the Tungsten probes used in the experimental characterizations can generate an unexpected resistive behaviour. In addition, the section in which the current flows in the real structure is reduced by the current crowding, leading to an increase of

the resistance.

- The combination of the uncertainty given by the lateral composition fluctuations inside the wells and the effect of the current crowding can easily affect the shape of the measured EL spectra. In fact, In clusters can form near the edges of the mesa structures where the current flow is intensified by the current crowding effect, leading to an unwanted red shift. 2D simulations are suggested in case of evident current crowding and low composition quality of the QWs. Researchers are also performing atomistic simulations to reproduce the tendency of In atoms to form clusters inside the wells.
- The band gap renormalization brought by the coulombian interactions in the QWs is a mandatory feature in order to match the modeled EL spectra with the measures in GaN-based LEDs. Nonetheless, the In molar fraction in the wells and the thicknesses of the QWs have an relevant impact on the EL spectra. A combination of values which brings to the EL superposition can be found exploiting all the parameters described.
- The unexpected thermal dependence of the measured EL spectra has been associated to a different set of problems. The electron overflow to the p-GaN cladding layer at low temperatures can justify the presence of a secondary peak related to the Mg acceptor level, while it can only partially justify the growing efficiency for higher temperatures and current injection. Other explanations are related to the dependence of the ballistic leakage with the temperature and its correlation to the thickness of the active regions.
- The matching of the EL spectra in GaN-based solar cells gives significant information about the quality of the complex active regions, made of tens of QWs. It should be always adopted as a preliminary study before a deeper investigation. We have seen how a thickness of the QWs below 3nm should not be considered for a proper quality of the active regions.
- The effect of the EBL inside a GaN-based solar cell has been questioned by the decrease in terms of simulated performances under AM1.5g illumination. The inconsistency between the experimental results and the model should be blamed on the validity of the simulations at low biases, where the

working region of the solar cells is situated. The incorporation of a tunneling transport model should be contemplated in presence of high potential barriers and deep QWs to achieve higher currents at low voltages.

InAlGaN material properties

A.1 Lattice structure

GaN, InN, AlN and the relative alloys are the compounds used in the micro-electronic devices here analysed. They can crystallize in both wurtzite and zinc-blende lattice forms, but it is the first one to be the most common, also in our case. We can appreciate its structure in Fig. A.1. The following data are necessary in order to reproduce the primitive cell: space group P63mc ($a = b \neq c$, $\alpha = \beta = 90^\circ$, $\gamma = 120^\circ$), Ga³⁺ position: $[\frac{1}{3} \frac{2}{3} \frac{1}{2}]$, N³⁻ position: $[\frac{1}{3} \frac{2}{3} \frac{7}{8}]$.

A.1.1 Polarization charges at the interfaces

Since the bonds between Ga and N atoms are partially ionic, the electron cloud is located closer to the N atoms, leading to negatively charged N atoms and positively charged Ga atoms. This phenomenon turns into the spontaneous polarization electric field in the crystallographic orientation [0001], because the charge neutrality is not satisfied at the interfaces. This phenomenon is directly related to the presence of two stacks of different atoms in the [0001] direction, where one stack is related to Ga ions and the second one to N ions as it can be seen in Fig. A.1.b. The spontaneous polarization electric field plays a significant role for III-nitride LEDs with the QW technology. The built-in electric field tilts the band structure of the QWs, leading to the separation of the electron from the hole wavefunctions and reducing the overlap of the electrons and holes, consequentially compromising the IQE. This effect is known as the quantum confined Stark

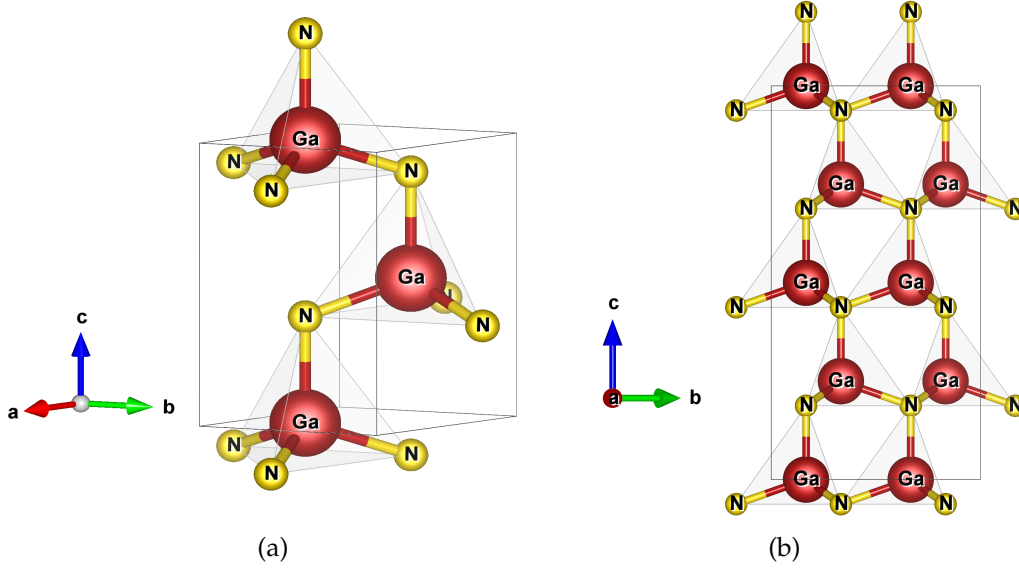


Figure A.1: (a) Primitive cell of wurtzite GaN with nearest N atoms bounded. (b) Super-lattice in parallel projection with respect to *a* direction. Both crystal morphologies are produced using the 3D visualization program for structural models VESTA (Visualization of Electronic and STructural Analysis).

effect (QCSE).

Moreover, the presence of hetero-junctions in GaN-based micro-electronic devices induces the so-called piezoelectric polarization. The charges generated at the interfaces InGaN/GaN, AlGaIn/GaN are the consequence of strain related to the lattice constant mismatch between the two compounds. The variation of the lattice constant with the composition is reported in Fig. A.2.

The polarization charges for nitride alloys of arbitrary composition had been modelled by *Fiorentini et al* [4]. The formulation of the spontaneous polarization, in C/m², is defined as:

$$\begin{aligned}
 P_{Al_xGa_{1-x}N}^{sp} &= -0.090x - 0.034(1-x) + 0.019x(1-x) \\
 P_{In_xGa_{1-x}N}^{sp} &= -0.042x - 0.034(1-x) + 0.038x(1-x) \\
 P_{Al_xIn_{1-x}N}^{sp} &= -0.090x - 0.042(1-x) + 0.071x(1-x)
 \end{aligned} \tag{A.1}$$

where the first two terms are the linear interpolation between the binary compounds while the third is the so-called bowing term. The piezoelectric polariza-

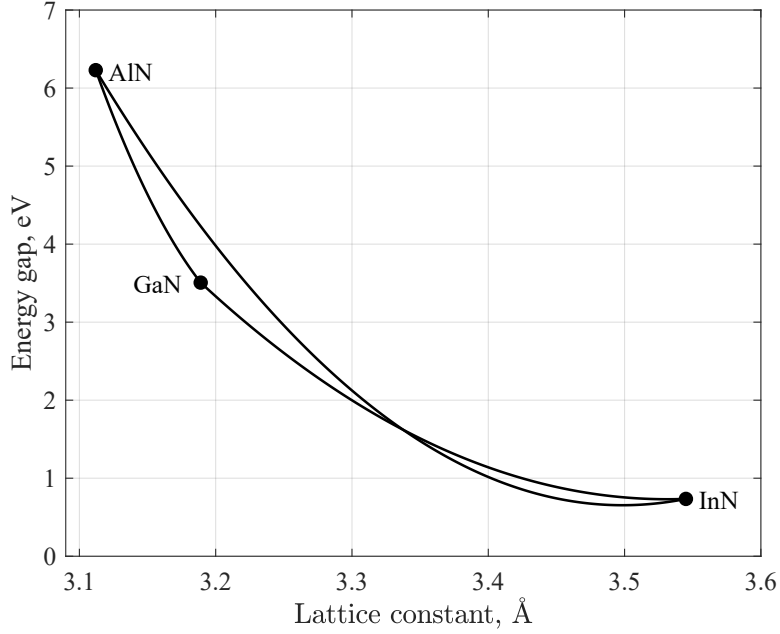


Figure A.2: Lattice constant vs energy gap of GaN, InN, AlN and the alloys.

tion of a generic alloy is defined with the Vegard interpolation:

$$\epsilon(x) = \frac{a_{subs} - a(x)}{a(x)} \quad (\text{A.2})$$

$$P_{X_xY_{1-x}N}^{pz}(x) = xP_{XN}^{pz}[\epsilon(x)] + (1-x)P_{YN}^{pz}[\epsilon(x)]$$

where $\epsilon(x)$ is the basal strain with $a(x)$ and a_{subs} being the lattice constants of the unstrained alloy and the substrate. P_{XN}^{pz} and P_{YN}^{pz} have the following quadratic dependence on the basal strain:

$$\begin{aligned} P_{AlN}^{pz} &= -1.808\epsilon + 5.624\epsilon^2 & \epsilon < 0 \\ P_{AlN}^{pz} &= -1.808\epsilon - 7.888\epsilon^2 & \epsilon > 0 \\ P_{GaN}^{pz} &= -0.918\epsilon + 9.541\epsilon^2 \\ P_{InN}^{pz} &= -1.373\epsilon + 7.559\epsilon^2 \end{aligned} \quad (\text{A.3})$$

Given the two types of polarization charges, the simulator gives the possibility to change the global amount with the screening factor x_{pol} [11] [29]:

$$P_z = -x_{pol} \left[P_{X_xY_{1-x}N}^{sp} + P_{X_xY_{1-x}N}^{pz} \right] \quad (\text{A.4})$$

where P_z is the global polarization considered in the [0001] direction.

A.2 Bandgap

The reason why the nitrides are interesting in the field of LEDs and solar cells applications is the tunability of the energy gap in a wide range (see Fig. A.2). However this important property comes with the limitation of highly strained interfaces, as said in the previous section. For what concerns the temperature dependence of the energy gap the Varshni formula is evaluated by:

$$E_g(T) = E_g|_{0K} - \frac{\alpha T^2}{T + \beta} \quad (\text{A.5})$$

α , β and the energy gap at null temperature of the three nitrides are listed in table B.2. The extreme values of temperature in the reliability analysis of the acspLED are 120 K and 350 K and in fig. A.3 the variation of the nominal energy gap of GaN and InN shows the importance of this dependence.

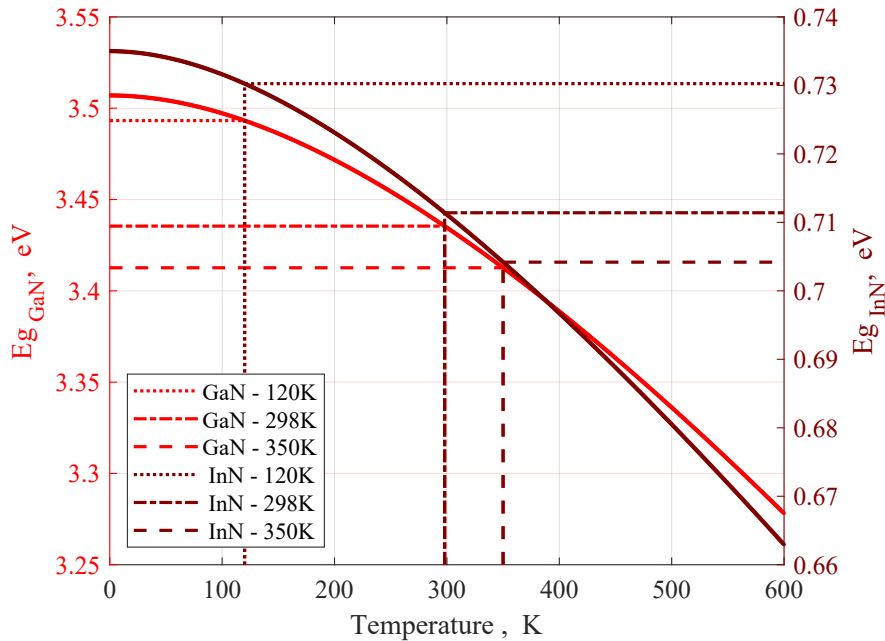


Figure A.3: GaN and InN energy gaps versus temperature. Dotted lines, energy gaps at the lower temperature achieved during reliability test. Dashed lines, energy gaps at room temperature. Dot-dashed lines, energy gaps at the highest experimental temperature.

The composition dependence of the energy gap for the ternary alloys AlGaN, InGaN, AlInN are described by the bowing equation A.6 at $T = 300\text{ K}$. The bowing parameter b accounts for the deviation from a linear interpolation between the two binary compounds (All parameters listed in table B.2).

$$\begin{aligned}
 E_g(\text{InGaN}) &= (1 - x_{\text{In}})E_g(\text{InN}) + xE_g(\text{GaN}) - x_{\text{In}}(1 - x_{\text{In}})b_{\text{InGaN}} \\
 E_g(\text{AlGaN}) &= (1 - x_{\text{Al}})E_g(\text{AlN}) + xE_g(\text{GaN}) - x_{\text{Al}}(1 - x_{\text{Al}})b_{\text{AlGaN}} \\
 E_g(\text{AlInN}) &= (1 - x_{\text{Al}})E_g(\text{AlN}) + xE_g(\text{InN}) - x_{\text{Al}}(1 - x_{\text{Al}})b_{\text{AlInN}}
 \end{aligned} \tag{A.6}$$

The energy gap decreases as the concentration increases since the bowing param-

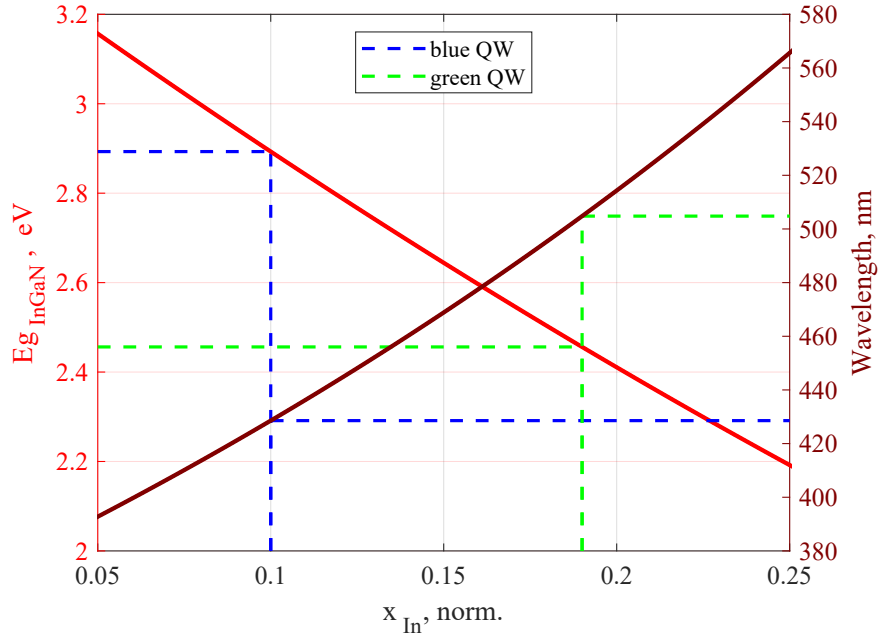


Figure A.4: InGaN nominal energy gap and related emission wavelength as a function of In concentration. Blue dashed line: $x_{\text{In}} = 0.10$, $E_g|_{\text{InGaN}} = 2.90\text{ eV}$, $\lambda|_{\text{InGaN}} = 427.3\text{ nm}$. Green dashed line: $x_{\text{In}} = 0.19$, $E_g|_{\text{InGaN}} = 2.46\text{ eV}$, $\lambda|_{\text{InGaN}} = 503.5\text{ nm}$.

eter is positive for all the three alloys. This behaviour is the key for the generation of heterostructures in opto-electronics. In fig. A.2 the energy gaps of the wurtzite nitrides are plotted as a function of the lattice constant. The concavity of the lines connecting the binary compounds is related to the magnitude of the bowing factor, indeed the curve related to the AlInN alloy has a bigger positive second derivative and also a bigger bowing factor with respect to the other two alloys.

Since our heterostructures are made of InGaN/GaN MQWs, the behaviour of the nominal energy gap of the InGaN alloy and the related wavelength of emission is described apart in Fig. A.4. A small range of In concentrations is presented in order to cover only the values of our active regions. Also the concentrations related to the two QWs in the LED structures are highlighted. In fact, the two nominal energy gaps are the initial step to understand the effect of the energies of the confined states on the spectrum of spontaneous emission, see section 1.2.2 for more details.

A.3 GaN crystal growth techniques

One of the main problems of GaN and its alloys is the absence of a substrate made of the native material; this is because N has a low solubility in Ga and its vapour pressure is higher with respect to GaN at the growth temperature of the crystal. Therefore, different kinds of substrate are chosen depending on the application, some examples follow. SiC has a small lattice mismatch with respect to the GaN and a good thermal conductivity. The sapphire has an important lattice mismatch with respect to GaN, however the growth of high efficiency electronic devices is possible with an intermediate buffer layer in order to compensate the mismatch. This is the case of our structures where a thick layer of undoped GaN crystal has been deposited on top of the sapphire substrate before building the main device. The last and most obvious choice is Si, the most used material in electronics and therefore the most cheap. However, we have to consider that the presence of a Si substrate introduces an evident lattice mismatch and an high difference between the coefficients of thermal expansion.

When the kind of substrate is selected the GaN crystal is deposited on top using different techniques:

- HVPE, *Hydride Vapour Phase Epitaxy*, is the first technique used to grow AlN and to allow deposition of GaN crystal with enough purity for electronic applications. This method is based on a flux of hydrides of the V group elements called the precursors, and a flux of hydrogen chloride in combination with nitrogen inside the furnace. Typically, there is a section dedicated to the sources, a mixing section and an area for the deposition. The thickness

of the deposited layer is in the range of 50:150 μm , making this process a good choice for the thick buffer layer on top of the substrate.

- MOCVD, *Metal Organic Chemical Vapour Deposition*, is based on the chemical reaction between a flux composed by the reactants in gas phase and the heated substrate. This process is mainly used for a fast and accurate deposition of hetero-structures made by III-V semiconductors. The reaction related to the deposition of GaN is: $\text{Ga}(\text{CH}_3)_3 + \text{NH}_3 \rightarrow \text{GaN} + 3\text{CH}_4$. High temperatures are required ($> 1000^\circ\text{C}$) for the GaN, while in the case of InN the temperature is near 500°C because of its smaller dissociation energy.
- MBE, *Molecular Beam Epitaxy*, exploits high vacuum to generate molecular layers by the injection of certain quantities of elements with a molecular beam. The composition and doping of the layer depend on the setting of the molar fraction for each molecular beam involved. The degree of epitaxial growth is controlled with RHEED, *Reflection High-Energy Electron Diffraction*, where an electron beam is focused on the surface of the growing lattice. Electrons with a small incidence angle and high energy are diffused only by the first layers of the material, for this reason, this technique is highly dependent on the surface crystallinity. Then the diffused electrons are detected by a sensor and the diffraction image of the surface of the crystal is generated. In this way the purity of each atomic layer of the lattice and its degree of crystallinity can be checked directly.

A.4 GaN doping process

The gallium nitride has an intrinsic n doping with a carrier concentration of 10^{16} cm^{-3} . Some studies give the responsibility of this post-fabrication donor behaviour to the presence of nitrogen vacancies that generate deep energy levels leading to the GaN yellow band. According to other studies, the n doping and the yellow band are also related to the presence of Si, Ge, O impurities. In any case, the presence of an intrinsic doping is an issue because of its uncontrollable fluctuations. Si or Ge are the n doping elements used in doping process of GaN that become substitutional atoms in the Ga lattice sites of the undoped crystal.

Instead the p doping is obtained with Mg. The fabrication of p doped GaN is challenging because of the compensation given by the intrinsic n doping and of the passivation brought by the H atoms. Therefore, the dissociation of the hydrogen bonded to the Mg atoms by heating is mandatory to achieve an higher dopant activation. This is possible with the application of the so called LEEBI, *Low Energy Electron Beam Irradiation*.

A.5 Contact development

The development of the ohmic contacts in the electronic devices is a primary process. As a matter of fact, an imperfection in the back-end section of the device can lead to an useless IV characteristic measurement, as happened in the case of two set of Color-Coded LED data, where a shift of some volts was associated to a malfunction of the contact pads. About the contact technology, in the case of n contact there is no metal with a work function so small to have a good ohmic contact with the GaN and, as a consequence, a thin depletion region is generated by a huge amount of GaN doping to exploit the tunneling at the interface between the contact itself and the n-doped GaN. Some improvements in this area have been achieved using multiple layers of Ti/Al and contacts with Ti/Al/Ni/Au, where the main problem is the presence of H atoms. For p type contacts, a small resistivity is a problematic requirement, because of the high energy gap of the GaN and the low hole concentration caused by a small activation of the Mg. The most common technique is a Ni/Au system. A thermal annealing in molecules of oxygen and nitrogen is a good improvement since the formation of a p type semiconductor NiO generates a thin Schottky barrier with the p GaN.

Theory behind the simulations

B.1 Drift-diffusion model

The equations used to describe the semiconductor device behaviour are Poisson's equation and the current continuity equations of electrons and holes. The former is derived from the Maxwell's equations and it is used to determine the potential and field distribution caused by a charge density within the depletion layer. Qualitatively the net change of carrier concentration is the difference between generation and recombination plus the net current flowing in and out between the two contacts of the device. These three main equations of the DD model are reported below:

$$\begin{cases} -\nabla(\epsilon\nabla\phi) = q(p - n + N_D^+ - N_A^-) + \rho_{pol} \\ \frac{\partial n}{\partial t} = \frac{1}{q}\nabla \cdot \mathbf{J}_n + G_n - R_n \\ \frac{\partial p}{\partial t} = -\frac{1}{q}\nabla \cdot \mathbf{J}_p + G_p - R_p \end{cases} \quad (\text{B.1})$$

Where ϵ is the dielectric constant of the material, ϕ the electrostatic potential of the device, q the electron charge, p and n are the carrier densities per unit of volume of the holes and the electrons, N_D^+ and N_A^- the concentrations of ionized doping atoms, ρ_{pol} is the polarization charge density, \mathbf{J}_n and \mathbf{J}_p are the current densities per unit of surface, G_n, R_n, G_p, R_p are the generation and recombination rate for electrons and holes.

The most common constitutive relation for the current density involves the

drift component, caused by the electric field, and the diffusion component, caused by the carrier concentration gradient. Together they generate the current-density equations B.2.

$$\begin{aligned}\mathbf{J}_n &= q\mu_n n E + qD_n \nabla n \\ \mathbf{J}_p &= q\mu_p p E - qD_p \nabla p\end{aligned}\tag{B.2}$$

μ_n and μ_p are the electron mobility and hole mobility, E is the applied electric field, D_n and D_p are the carrier diffusion constants. In case of a nondegenerate semiconductor the carrier diffusion constants are given by the Einstein relation (see eq. B.3) where K_B is the Boltzmann constant and T is the temperature of the material.

$$D_n = \frac{K_B T}{q} \mu_n \quad D_p = \frac{K_B T}{q} \mu_p\tag{B.3}$$

B.1.1 Damped Newton method

The DD model is solved by means of self-consistent numerical approach since a closed form solution cannot be evaluated. The iterative process can be solved with respect to the carrier concentrations or the quasi-Fermi levels. This feature is present because the solution at low bias is difficult to obtain with the default variables: potential and quasi-Fermi levels. In other words, the current is so small under high resistance that the solution cannot converge to proper values of the quasi-Fermi levels [11].

The boundary conditions for the solution of equation B.1 are the ohmic contacts. They are implemented as Dirichlet boundary conditions, where the potential and the quasi-Fermi levels are fixed and set to the applied bias.

The applied numerical process is the Newton method. The starting point is the approximation of the electrostatic potential profile, then the two carrier concentrations are evaluated. The third step requires the Poisson's equation, where the concentrations are given as input and the electrostatic potential is the output. The iterative procedure is applied until convergency is reached, meaning that the difference between the carrier concentrations of two consecutive steps is less than a defined threshold. If the quantum confinement is present in the device, as in our case, the Schrödinger equation is added to the system giving a third carrier concentration (see appendix B.2 for further details).

Table B.1: Parameters of the damped Newton method.

<i>Damping step</i>	5
<i>Tolerance of the variable</i>	$10^{-6} : 10^{-2}$
<i>Tolerance of the residual</i>	$10^{-6} : 10^{-2}$
<i>Maximum number of iterations</i>	100
<i>Optimal number of iterations</i>	15 : 65

The simulations performed in this work have approximately all the same parameters used for the Newton method (see table B.1) thanks to the fact that the simulated structures are only lightly different from each other. The *damping step* represents the application of the Bank-Rose algorithm to the Newton method [51]. As the name should suggests, the *damping step* helps the simulation to reach convergency by decreasing the step size when the variables at each iteration start to loss the convergent trend. However a the smaller this parameter is set, the slower will be the self-consistent method. The *tolerance of the variable* and the *tolerance of the residual* are the lower limits beyond which the solution is considered converged, whereas the *maximum number of iterations* defines the upper limit of iterations. If the required number is greater, the solution is not found and a new procedure will automatically start with a smaller step size. The program adjusts the step size by following the *optimal number of iterations* [11].

B.2 Self-consistent carrier density model

In order to understand the application of the quantum correction made to the DD model we will start by considering the eigenvalue formulation of the Schrödinger equation (see equation B.4).

$$\left[\hat{H}(r, k) + \hat{V}(r) \right] \Psi(r, k) = E(r, k) \Psi(r, k) \quad (\text{B.4})$$

Where $\hat{H}(r, k)$ is the Hamiltonian, $\hat{V}(r)$ is the potential energy, $\Psi(r, k)$ the eigenfunctions and $E(r, k)$ the eigenvalues. The $k\hat{p}$ approximation of the Schrödinger equation is joint to the Poisson's equation when considering the quantum corrected DD model. In other words, $\hat{V}(r)$ resembles ϕ and the charge density is

evaluated from the eigenfunctions. A new value of electrostatic potential closes the self-consistent loop [29].

The basic method to find the quantum confined states in the quantum well is based on assuming to deal with a piece-wise constant potential, *i.e.*, flat-band condition. Therefore, the variation of potential, due to any kind of electric field in the quantum well, is assumed to be small enough that the energy mismatch between the two interfaces is negligible. However, in presence of piezoelectric field as in InGaN/GaN hetero-structures the quantum well is heavily tilted to one-side. The confined wave function will have an asymmetric shape and the current flow will be affected leading to a decrease of device performance, as mentioned in appendix A. Therefore, a self-consistent model is applied. The initial potential distribution is given by solving at equilibrium with flat-band approximation. Successively the potential is solved again at equilibrium applying the potential obtained before and using the self-consistent density model shown in eq. B.5 for electrons.

$$n_{2D}(x, y) = \sum_j g_n^j(y) \rho_j^0 k_B T \ln[1 + e^{(E_{fn}(x) - E_j)/(k_B T)}] \quad (\text{B.5})$$

Where the well is assumed to be parallel to the \vec{x} direction, $g_n^j(y)$ is the electron wave function, E_j is the energy of the confined level, ρ_j^0 is the 2D density of states. This step is repeated until self-consistency is achieved. As a final part of the cycle, the bias is increased and the process restarted. It is easily understandable how this method can require an higher computational cost. Nonetheless, the solution of the Schrödinger equation has to be performed for each quantum well since the local potential could change.

In order to use the iterative method, boundary conditions are mandatory. the analytical solutions decay to zero at infinity. While the numerical solutions are reached by means of a certain fixed wave range. Therefore, the wave functions are truncated to zero by an infinite potential well symmetric or not with respect to the center of the quantum well. In our simulations this range is symmetrical and the values used for the simulations are reported in the main chapters.

B.3 ABC model

The loss mechanisms inside the junction are modeled by the so-called ABC model. Each letter of the name represents one particular parametrized loss mechanism, in the next three sections will follow more explanations. The amount of leakage in terms of current, given by one specific contribute, is correlated to the carrier density profile as follows:

$$\mathbf{J}_{loss} = An + Bn^2 + Cn^3 + \mathbf{J}_{rest} \quad (\text{B.6})$$

where A , B and C are the Shockley-Read-Hall (SRH), the spontaneous emission and the Auger coefficient, respectively. \mathbf{J}_{rest} takes into account the probability to have non-capture or escape from the QW.

B.3.1 SRH recombination rate

The Shockley-Read-Hall (SRH) recombination is a non-radiative process given by deep level traps inside the energy gap of the semiconductor. The energy traps are associated to the density of defects in the crystalline structure. The model used is the following:

$$\begin{aligned} R_n^{tj} &= c_{nj}nN_{tj}(1 - f_{tj}) - c_{nj}n_{1j}N_{tj}f_{tj} \\ R_p^{tj} &= c_{pj}pN_{tj}f_{tj} - c_{pj}p_{1j}N_{tj}(1 - f_{tj}) \end{aligned} \quad (\text{B.7})$$

Where c_{nj} and c_{pj} are the capture coefficients for electrons and holes and are related to the lifetime of the carriers of the j th trap as shown in equation B.8. Moreover, the capture coefficients of each trap are directly proportional to the thermal velocity of the carriers, where the coefficients of proportionality are the capture cross sections of the trap (see equation B.8). n_{1j} is the electron concentration when the quasi-Fermi level of the electrons is superposed with the energy level E_{tj} of the considered trap, same formalism for p_{1j} . Finally, N_{tj} is the trap density [11].

$$\begin{aligned} A_n &= \frac{1}{\tau_{nj}} = c_{nj}N_{tj} = \sigma_{nj}v_nN_{tj} = \sigma_{nj}\sqrt{\frac{8kT}{\pi m_n}}N_{tj} \\ A_p &= \frac{1}{\tau_{pj}} = c_{pj}N_{tj} = \sigma_{pj}v_pN_{tj} = \sigma_{pj}\sqrt{\frac{8kT}{\pi m_p}}N_{tj} \end{aligned} \quad (\text{B.8})$$

B.3.2 Radiative recombination rate

Radiative recombination is a process that involves band-to-band transitions that cause the production of photons with energy related to the gap between the initial state in the conduction band and the final state in the valence band. The expression for the bulk layers of the structure is given by:

$$R_{rad}^b = B(np - n_i^2) \quad (\text{B.9})$$

where n_i is the intrinsic carrier concentration. For the active region, the radiative rate is resolved in energy in order to generate the EL intensity and is computed as follows:

$$R_{rad}^{qw}(E) = \left(\frac{2\pi}{\hbar}\right) \left(\frac{e}{m_0}\right)^2 \left(\frac{2\hbar\omega}{4\epsilon\omega^2}\right) |M_{avg}|^2 \rho_{red}(E) D(E) f_c(1 - f_v) \quad (\text{B.10})$$

where the average momentum matrix is expressed as:

$$|M_{avg}|^2 = \frac{m_0}{6} \left(\frac{m_0}{m^*} - 1\right) \frac{E_g(E_g + \Delta_{so})}{\left(E_g + \frac{2}{3}\Delta_{so}\right)} \quad (\text{B.11})$$

in which m^* is the effective mass of the carriers and Δ_{so} is the spin-orbit splitting energy of the valence band. $D(E)$ is the optical mode density:

$$D(E) = \frac{n^3 E^2}{\pi^2 \hbar^3 c^3} \quad (\text{B.12})$$

with n being the refractive index of the material. Finally, $\rho_{red}(E)$ is the density of states evaluated with the reduced effective mass $m_{red} = (m_e m_h)/(m_e + m_h)$. For more details about the computation of the radiative recombination rate starting from the primary principles we suggest to consider the references [52], [11]. As a last remark, it is significant to give a brief explanation of the unit of magnitude of the spontaneous emission rate, because the literature typically overcomes this part of theory by normalizing physical quantity. Therefore, the spontaneous emission rate is computed in $[\text{s}^{-1}\text{m}^{-1}\text{eV}^{-1}]$, where the m is caused by the type of simulations we are performing; as a matter of fact our simulations are 1D but the thickness of one of the two transversal directions is given, meaning that only one transversal dimension is not considered by the physical quantities. While the eV

is given by the optical mode density.

B.3.3 Auger recombination rate

The Auger recombination is a non-radiative process in which the energy produced by the recombination of an e-h pair is acquired by a third carrier. The described phenomenon is the so-called direct Auger recombination. The third carrier can be assisted by lattice vibration through an electron-phonon coupling, leading to the indirect Auger recombination. The formula used for the evaluation of the rate is given by:

$$R_{au} = (C_n n + C_p p)(np - n_i^2) \quad (\text{B.13})$$

where C_n and C_p are the Auger coefficients and n_i is the intrinsic carrier concentration [11].

B.4 Generation rate

The carrier generation rate is defined as the number of carriers generated by the incident light source per unit of time and can be evaluated using the following formula:

$$G(y) = \int_0^{\lambda_{gap}} \alpha(\lambda) T(\lambda) N_{ph}(\lambda) e^{-\alpha(\lambda)y} d\lambda \quad (\text{B.14})$$

where $\alpha(\lambda)$ is the semiconductor absorption coefficient, $T(\lambda)$ is the transmittance into the semiconductor, y is the considered depth of the sample and $N_{ph}(\lambda)$ is the incident photon flux, that is evaluated as:

$$N_{ph}(\lambda) = \frac{P_{op}(\lambda)}{\hbar\omega} \quad (\text{B.15})$$

where $\hbar\omega$ is the energy of a single photon with a certain wavelength and $P_{op}(\lambda)$ is the spectral irradiance, which takes into account the amount of photons arriving at the solar cell surface per unit of time, in relation to the wavelength. For what concerns the absorption coefficient, it is a major parameter that decides at which material depth the light with a particular wavelength can penetrate before it is absorbed. This coefficient depends on the material and the wavelength.

B.5 Incomplete ionization of impurities

The magnitude of the ionization in a doped semiconductor is defined by the two occupancy functions f_D and f_A , one for each type of doping (see equation B.16).

$$\begin{aligned} f_D &= \frac{1}{1 + g_d^{-1} e^{(E_D - E_{fn})/(k_B T)}} = \frac{N_D^+}{N_D} \\ f_A &= \frac{1}{1 + g_a e^{(E_A - E_{fp})/(k_B T)}} = \frac{N_A^-}{N_A} \end{aligned} \quad (\text{B.16})$$

g_d and g_a are the degeneracy number of donors and acceptors. Their default values are 4 and 2, respectively [11]. E_D and E_A are the activation energies of donors and acceptors. E_{fn} and E_{fp} are the electron and hole quasi-Fermi levels. N_D^+/N_D and N_A^-/N_A are the fraction of ionized dopants for each doping type.

B.6 GaN, InN, AlN parameter collection

This section is a summary of the parameters used in all the simulations done (see table B.2), therefore the changes belonging to each singular simulation are just given in the relative section, always in form of tables. Here follows a brief overview of the parameters presented: a and c are the lattice constants, E_g is the energy gap, α and β are the coefficients of the Varshni model for the temperature dependence of E_g , χ is the electron affinity, Δ_{so} and Δ_{cr} are the spin-orbit and crystal-field splitting energies, ε is the relative dielectric constant, m_e^{\parallel} and m_e^{\perp} are the longitudinal and transverse components of the electron effective mass, $A_1 \dots A_6$ are the Luttinger parameters of the $k \cdot p$ Hamiltonian, $D_1 \dots D_6$ are the valence band deformation potentials, $c_{11} \dots c_{44}$ are the elastic constants for wurtzite materials, $\mu_{n|p}$ are the electron and hole mobilities assumed to be independent of temperature, ionized impurity densities, and In molar fraction.

For what concerns the set of luttinger parameters, we have to say that the valence bands of the zinc-blende structure can be described by three Luttinger parameters and the spin-orbit splitting. While in the wurtzite case the number of Luttinger parameters must be increased because of the lower symmetry of the lattice.

Table B.2: Material parameters of GaN, InN and AlN.

Parameter	GaN	InN	AlN
$a, \text{Å}$	3.1892	3.5446	3.112
$c, \text{Å}$	5.185	5.718	5.185
E_g at $T = 0\text{K}$, eV	3.507	0.735	6.23
$\alpha, \text{meV K}^{-1}$	0.909	0.245	1.799
β, K	830	624	1462
χ, eV	4.07	5.9272	0.6
Δ_{so}, meV	14	1	...
Δ_{cr}, meV	19	41	...
ε	9.5	15	8.5
m_e^{\parallel}	0.20	0.12	0.32
m_e^{\perp}	0.20	0.12	0.28
A_1	-6.56	-8.21	...
A_2	-0.91	-0.68	...
A_3	5.65	7.57	...
A_4	-2.83	-5.23	...
A_5	-3.13	-5.11	...
A_6	-4.86	-5.96	...
D_1, eV	-3.0	-3.0	...
D_2, eV	3.6	3.6	...
D_3, eV	8.82	8.82	...
D_4, eV	-4.41	-4.41	...
D_5, eV	-4.0	-2.33	...
D_6, eV	-5.0770	-0.3536	...
c_{11}, GPa	390	271	...
c_{12}, GPa	145	124	...
c_{13}, GPa	106	92	...
c_{33}, GPa	398	224	...
c_{44}, GPa	105	46	...
$\mu_n, \text{cm}^2 \text{V}^{-1} \text{s}^{-1}$	300	300	300
$\mu_p, \text{cm}^2 \text{V}^{-1} \text{s}^{-1}$	10	10	10

Bibliography

- [1] W. Lee, J.-H. Choi, S. Ryu, D. Jung, J. Song, J.-S. Lee, and C. Joo, “Color-coded LED microscopy for quantitative phase imaging: Implementation and application to sperm motility analysis”, *Methods*, vol. 136, Nov. 2017. DOI: [10.1016/j.ymeth.2017.11.010](https://doi.org/10.1016/j.ymeth.2017.11.010).
- [2] E. Dogmus, M. Zegaoui, L. Largeau, M. Tchernycheva, V. Neplokh, S. Weiszer, F. Schuster, M. Stutzmann, M. Foldyna, and F. Medjdoub, “High structural quality InGaN/GaN multiple quantum well solar cells”, *physica status solidi (c)*, Aug. 2015. DOI: [10.1002/pssc.201510137](https://doi.org/10.1002/pssc.201510137).
- [3] Z. Bi, J. Zhang, Q. Zheng, L. Lv, Z. Lin, H. Shan, P. Li, X. Ma, Y. Han, and Y. Hao, “An InGaN based solar cell including dual InGaN/GaN multiple quantum wells”, *IEEE Photonics Technology Letters*, vol. 28, pp. 1–1, Oct. 2016. DOI: [10.1109/LPT.2016.2575058](https://doi.org/10.1109/LPT.2016.2575058).
- [4] V. Fiorentini, F. Bernardini, and O. Ambacher, “Evidence for nonlinear macroscopic polarization in III–V nitride alloy heterostructures”, *Applied Physics Letters*, vol. 80, pp. 1204–1206, Feb. 2002. DOI: [10.1063/1.1448668](https://doi.org/10.1063/1.1448668).
- [5] M. Mandurrino, G. Verzellesi, M. Goano, M. Vallone, F. Bertazzi, G. Ghione, M. Meneghini, G. Meneghesso, and E. Zanoni, “Physics-based modeling and experimental implications of trap-assisted tunneling in InGaN/GaN light-emitting diodes”, *physica status solidi (a)*, vol. 212, May 2015. DOI: [10.1002/pssa.201431743](https://doi.org/10.1002/pssa.201431743).

-
- [6] V. K. Malyutenko, S. S. Bolgov, and A. D. Podoltsev, "Current crowding effect on the ideality factor and efficiency droop in blue lateral InGaN/GaN light emitting diodes", *Applied Physics Letters*, vol. 97, no. 25, p. 251110, 2010. DOI: [10.1063/1.3529470](https://doi.org/10.1063/1.3529470).
- [7] E. F. Schubert, *Light-Emitting Diodes*, 2nd. Cambridge, U.K.: Cambridge University Press, 2006.
- [8] A. Billeb, W. Grieshaber, D. Stocker, E. Schubert, and R. Karlicek Jr, "Microcavity effects in GaN epitaxial films and in Ag/GaN/sapphire structures", *Applied Physics Letters*, vol. 70, pp. 2790–2792, May 1997. DOI: [10.1063/1.119060](https://doi.org/10.1063/1.119060).
- [9] J. Piprek, "How to decide between competing efficiency droop models for GaN-based light-emitting diodes", *Applied Physics Letters*, vol. 107, no. 3, p. 031101, 2015. DOI: [10.1063/1.4927202](https://doi.org/10.1063/1.4927202).
- [10] M. Calciati, M. Goano, F. Bertazzi, M. Vallone, X. Zhou, G. Ghione, M. Meneghini, G. Meneghesso, E. Zanoni, E. Bellotti, G. Verzellesi, D. Zhu, and C. Humphreys, "Correlating electroluminescence characterization and physics-based models of InGaN/GaN LEDs: Pitfalls and open issues", vol. 4, no. 6, p. 067118, Jun. 2014. DOI: [10.1063/1.4882176](https://doi.org/10.1063/1.4882176).
- [11] *Crosslight device simulation software. general manual*, Crosslight Software Inc., Vancouver, BC, Canada, Sep. 2014.
- [12] Y. Kanitani, S. Tanaka, S. Tomiya, T. Ohkubo, and K. Hono, "Atom probe tomography of compositional fluctuation in GaInN layers", *Japanese Journal of Applied Physics*, vol. 55, no. 5S, 05FM04, Apr. 2016. DOI: [10.7567/jjap.55.05fm04](https://doi.org/10.7567/jjap.55.05fm04).
- [13] Y.-R. Wu, R. Shivaraman, k.-c. Wang, and J. Speck, "Analyzing the physical properties of InGaN multiple quantum well light emitting diodes from nano scale structure", *Applied Physics Letters*, vol. 101, p. 083505, Aug. 2012. DOI: [10.1063/1.4747532](https://doi.org/10.1063/1.4747532).
- [14] T. Kunikiyo, S. Hattori, R. Shirasawa, and S. Tomiya, "First-principles calculations of carrier localization in fluctuated InGaN quantum wells", *Japanese*
-

- Journal of Applied Physics*, vol. 58, SCCB05, Jun. 2019. DOI: [10.7567/1347-4065/ab0f18](https://doi.org/10.7567/1347-4065/ab0f18).
- [15] E. Kioupakis, Q. Yan, D. Steiauf, and C. Van de Walle, "Temperature and carrier-density dependence of auger and radiative recombination in nitride optoelectronic devices", *New Journal of Physics*, vol. 15, pp. 5006–, Dec. 2013. DOI: [10.1088/1367-2630/15/12/125006](https://doi.org/10.1088/1367-2630/15/12/125006).
- [16] I. Vurgaftman and J. R. Meyer, "Band parameters for nitrogen-containing semiconductors", vol. 94, no. 6, pp. 3675–3696, Sep. 2003. DOI: [10.1063/1.1600519](https://doi.org/10.1063/1.1600519).
- [17] H. P. Maruska and J. J. Tietjen, "The preparation and properties of vapor-deposited single-crystal-line gan", *Applied Physics Letters*, vol. 15, no. 10, pp. 327–329, 1969. DOI: [10.1063/1.1652845](https://doi.org/10.1063/1.1652845).
- [18] M. Leszczyński, H. Teisseyre, T. Suski, I. Grzegory, M. Bockowski, J. Jun, B. Palosz, S. Porowski, K. Pakuła, J. Baranowski, and A. Barski, "Thermal expansion of GaN bulk crystals and homoepitaxial layers", *Acta Physica Polonica A*, vol. 90, pp. 887–890, Nov. 1996. DOI: [10.12693/APhysPolA.90.887](https://doi.org/10.12693/APhysPolA.90.887).
- [19] C. De Santi, M. Meneghini, M. La Grassa, B. Galler, R. Zeisel, M. Goano, S. Dominici, M. Mandurro, F. Bertazzi, D. Robidas, G. Meneghesso, and E. Zanoni, "Role of defects in the thermal droop of InGaN-based light emitting diodes", vol. 119, no. 9, p. 094501, Mar. 2016. DOI: [10.1063/1.4942438](https://doi.org/10.1063/1.4942438).
- [20] A. Schenk, "A model for the field and temperature dependence of shockley-read-hall lifetimes in silicon", *Solid-State Electronics*, vol. 35, no. 11, pp. 1585–1596, 1992, ISSN: 0038-1101. DOI: [10.1016/0038-1101\(92\)90184-E](https://doi.org/10.1016/0038-1101(92)90184-E).
- [21] T. Lin, F. Wang, C.-H. Cheng, S. Chen, Z. C. Feng, and G.-R. Lin, "Strain-related recombination mechanisms in polar InGaN/GaN MQWs on amorphous SixC1-x buffers", *Opt. Mater. Express*, vol. 8, no. 5, pp. 1100–1106, 2018. DOI: [10.1364/OME.8.001100](https://doi.org/10.1364/OME.8.001100).

-
- [22] H. Nguyen, M. Djavid, K. Cui, and Z. Mi, "Temperature-dependent non-radiative recombination processes in GaN-based nanowire white-light-emitting diodes on silicon", *Nanotechnology*, vol. 23, p. 194 012, Apr. 2012. DOI: [10.1088/0957-4484/23/19/194012](https://doi.org/10.1088/0957-4484/23/19/194012).
- [23] Y. Da-Wei, "Temperature-dependent efficiency droop in GaN-based blue LEDs", *IEEE Electron Device Letters*, vol. PP, Feb. 2018. DOI: [10.1109/LED.2018.2805192](https://doi.org/10.1109/LED.2018.2805192).
- [24] P. Tian, J. J. D. McKendry, J. Herrnsdorf, S. Watson, R. Ferreira, I. M. Watson, E. Gu, A. E. Kelly, and M. D. Dawson, "Temperature-dependent efficiency droop of blue InGaN micro-light emitting diodes", *Applied Physics Letters*, vol. 105, no. 17, p. 171 107, 2014. DOI: [10.1063/1.4900865](https://doi.org/10.1063/1.4900865).
- [25] W. Chow, "Modeling of temperature and excitation dependences of efficiency in an InGaN light-emitting diode", *Optics express*, vol. 22, pp. 1413–25, Jan. 2014. DOI: [10.1364/OE.22.001413](https://doi.org/10.1364/OE.22.001413).
- [26] B. Pődör, "Thermal ionization energy of Mg acceptors in GaN: Effects of doping level and compensation", *Proceedings of SPIE - The International Society for Optical Engineering*, vol. 4412, p. 5, Aug. 2001. DOI: [10.1117/12.435848](https://doi.org/10.1117/12.435848).
- [27] F. Bertazzi, M. Goano, and E. Bellotti, "Numerical analysis of indirect Auger transitions in InGaN", vol. 101, no. 1, p. 011 111, Jul. 2012. DOI: [10.1063/1.4733353](https://doi.org/10.1063/1.4733353).
- [28] S. Brochen, J. Brault, S. Chenot, A. Dussaigne, M. Leroux, and B. Damilano, "Dependence of the Mg-related acceptor ionization energy with the acceptor concentration in p-type GaN layers grown by molecular beam epitaxy", *Applied Physics Letters*, vol. 103, no. 3, p. 032 102, 2013. DOI: [10.1063/1.4813598](https://doi.org/10.1063/1.4813598).
- [29] S. Dominici, "Numerical investigation of efficiency loss mechanisms in light emitting diodes", PhD thesis, Politecnico di Torino, 2017. DOI: [10.6092/polito/porto/2669184](https://doi.org/10.6092/polito/porto/2669184).
-

- [30] M. Mandurrino, G. Verzellesi, M. Goano, M. Vallone, F. Bertazzi, G. Ghione, M. Meneghini, G. Meneghesso, and E. Zanoni, "Physics-based modeling and experimental implications of trap-assisted tunneling in InGaN/GaN light-emitting diodes", vol. 212, no. 5, pp. 947–953, 2015. DOI: [10.1002/pssa.201431743](https://doi.org/10.1002/pssa.201431743).
- [31] G. Wang, X. Tao, J. Liu, and F. Jiang, "Temperature-dependent electroluminescence from InGaN/GaN green light-emitting diodes on silicon with different quantum-well structures", *Semiconductor Science and Technology*, vol. 30, no. 1, p. 015 018, Dec. 2014. DOI: [10.1088/0268-1242/30/1/015018](https://doi.org/10.1088/0268-1242/30/1/015018).
- [32] D.-S. Shin, D.-P. Han, J.-Y. Oh, and J.-I. Shim, "Study of droop phenomena in InGaN-based blue and green light-emitting diodes by temperature-dependent electroluminescence", *Applied Physics Letters*, vol. 100, no. 15, p. 153 506, 2012. DOI: [10.1063/1.3703313](https://doi.org/10.1063/1.3703313).
- [33] J. Han, G. Kang, D. Kang, Y. Moon, H. Jeong, J.-O. Song, and T.-Y. Seong, "Effect of different quantum well structures on the output power performance of GaN-based light-emitting diodes", *Journal of Electronic Materials*, vol. 42, pp. 2876–2880, Oct. 2013. DOI: [10.1007/s11664-013-2704-y](https://doi.org/10.1007/s11664-013-2704-y).
- [34] H. Long, T. J. Yu, L. Liu, Z. J. Yang, H. Fang, and G. Y. Zhang, "Different exciton behaviors in blue and green wells of dual-wavelength InGaN/GaN MQWs structures", *Journal of Applied Physics*, vol. 111, no. 5, p. 053 110, 2012. DOI: [10.1063/1.3692087](https://doi.org/10.1063/1.3692087).
- [35] L. Liu, L. Wang, N. Liu, W. Yang, D. Li, W. Chen, Z. Chuan Feng, Y.-C. Lee, I. Ferguson, and X. Hu, "Investigation of the light emission properties and carrier dynamics in dual-wavelength InGaN/GaN multiple-quantum well light emitting diodes", *Journal of Applied Physics*, vol. 112, no. 8, p. 083 101, 2012. DOI: [10.1063/1.4759373](https://doi.org/10.1063/1.4759373).
- [36] D. S. Meyaard, G.-B. Lin, Q. Shan, J. Cho, E. F. Schubert, H. Shim, M.-H. Kim, and C. Sone, "Asymmetry of carrier transport leading to efficiency droop in GaInN based light-emitting diodes", vol. 99, no. 25, p. 251 115, 2011. DOI: [10.1063/1.3671395](https://doi.org/10.1063/1.3671395).

-
- [37] B. Galler, A. Laubsch, A. Wojcik, H. Lugauer, A. Gomez-Iglesias, M. Sabathil, and B. Hahn, "Investigation of the carrier distribution in InGaN-based multi-quantum-well structures", vol. 8, no. 7–8, pp. 2372–2374, 2011. DOI: [10.1002/pssc.201001075](https://doi.org/10.1002/pssc.201001075).
- [38] A. Laubsch, M. Sabathil, J. Baur, M. Peter, and B. Hahn, "High-power and high-efficiency InGaN-based light emitters", vol. 57, no. 1, pp. 79–87, Feb. 2010. DOI: [10.1109/TED.2009.2035538](https://doi.org/10.1109/TED.2009.2035538).
- [39] M. Peter, A. Laubsch, W. Bergbauer, T. Meyer, M. Sabathil, J. Baur, and B. Hahn, "New developments in green LEDs", *physica status solidi (a)*, vol. 206, pp. 1125–1129, Jun. 2009. DOI: [10.1002/pssa.200880926](https://doi.org/10.1002/pssa.200880926).
- [40] D.-S. Kim and B. Han, "Effect of junction temperature on heat dissipation of high power light emitting diodes", *Journal of Applied Physics*, vol. 119, no. 12, p. 125 104, 2016. DOI: [10.1063/1.4944800](https://doi.org/10.1063/1.4944800).
- [41] P. Li, H. Li, Z. Li, J. Kang, X. Yi, J. Li, and G. Wang, "Strong carrier localization effect in carrier dynamics of 585 nm InGaN amber light-emitting diodes", *Journal of Applied Physics*, vol. 117, p. 073 101, Feb. 2015. DOI: [10.1063/1.4906960](https://doi.org/10.1063/1.4906960).
- [42] K. Kim, D. Meynard, G.-B. Lin, E. Schubert, J. K. Kim, and J. Cho, "Temperature dependence of efficiency in GaInN/GaN light-emitting diodes with a GaInN underlayer", *International Journal of Applied Ceramic Technology*, vol. 13, Sep. 2015. DOI: [10.1111/ijac.12483](https://doi.org/10.1111/ijac.12483).
- [43] I. Titkov, S. Karpov, A. Yadav, V. Zerova, M. Zulonas, B. Galler, M. Straßburg, I. Pietzonka, H.-J. Lugauer, and E. Rafailov, "Temperature-dependent internal quantum efficiency of blue high-brightness light-emitting diodes", *IEEE Journal of Quantum Electronics*, vol. 50, pp. 911–920, Sep. 2014. DOI: [10.1109/JQE.2014.2359958](https://doi.org/10.1109/JQE.2014.2359958).
- [44] D.-P. Han, J.-I. Shim, and D.-S. Shin, "Factors determining the carrier distribution in InGaN/GaN multiple-quantum-well light-emitting diodes", *IEEE Journal of Quantum Electronics*, vol. PP, May 2017. DOI: [10.1109/JQE.2018.2790440](https://doi.org/10.1109/JQE.2018.2790440).
-

- [45] P. Dalapati, N. Manik, and A. Basu, "Influence of temperature on different optoelectronic characteristics of InGaN light emitting diodes", *Optical and Quantum Electronics*, vol. 49, p. 265, Aug. 2017. DOI: [10.1007/s11082-017-1104-6](https://doi.org/10.1007/s11082-017-1104-6).
- [46] I. Prudaev, O. Tolbanov, and S. Khludkov, "Low-temperature transport of charge carriers in InGaN/GaN multiple quantum well light-emitting diodes", *physica status solidi (a)*, vol. 212, no. 5, pp. 930–934, 2015. DOI: [10.1002/pssa.201431646](https://doi.org/10.1002/pssa.201431646).
- [47] I. Prudaev, V. Kopyev, I. Romanov, and V. Brudnyi, "Temperature dependence of quantum efficiency of InGaN/GaN led structures at high current density", *Russian Physics Journal*, vol. 58, Sep. 2015. DOI: [10.1007/s11182-015-0545-2](https://doi.org/10.1007/s11182-015-0545-2).
- [48] C.-H. Wang, J. Chen, C.-H. Chiu, H.-C. Kuo, Y.-L. Li, T.-c. Lu, and S.-C. Wang, "Temperature-dependent electroluminescence efficiency in blue InGaN–GaN light-emitting diodes with different well widths", *IEEE Photonics Technology Letters*, vol. 22, Feb. 2010. DOI: [10.1109/LPT.2009.2037827](https://doi.org/10.1109/LPT.2009.2037827).
- [49] H. Wang, Y. Lin, L.-H. Zhu, Y. Lu, Y. Tu, Z. Liu, Z. Deng, W. Tang, Y. Gao, and Z. Chen, "Temperature dependent carrier localization in AlGaInN near-ultraviolet light-emitting diodes", *Optics Express*, vol. 24, p. 11 594, May 2016. DOI: [10.1364/OE.24.011594](https://doi.org/10.1364/OE.24.011594).
- [50] X. Huang, H. Chen, H. Fu, I. Baranowski, J. Montes, T.-H. Yang, K. Fu, B. P. Gunning, D. D. Koleske, and Y. Zhao, "Energy band engineering of InGaN/GaN multi-quantum-well solar cells via AlGaIn electron- and hole-blocking layers", *Applied Physics Letters*, vol. 113, no. 4, p. 043 501, 2018. DOI: [10.1063/1.5028530](https://doi.org/10.1063/1.5028530).
- [51] R. Bank and D. Rose, "Global approximate newton methods", *Numerische Mathematik*, vol. 37, pp. 279–295, Jan. 1981. DOI: [10.1007/BF01398257](https://doi.org/10.1007/BF01398257).
- [52] R. H. Yan, S. W. Corzine, L. A. Coldren, and I. Suemune, "Corrections to the expression for gain in GaAs", *IEEE Journal of Quantum Electronics*, vol. 26, no. 2, pp. 213–216, Feb. 1990. DOI: [10.1109/3.44950](https://doi.org/10.1109/3.44950).